Ideal boundary layer stability parameters for onshore tall-turbine wind farms

Sonia Wharton, Julie Lundquist

March 4, 2010

Wind Energy

Disclaimer

This document was prepared as an account of work sponsored by an agency of the United States government. Neither the United States government nor Lawrence Livermore National Security, LLC, nor any of their employees makes any warranty, expressed or implied, or assumes any legal liability or responsibility for the accuracy, completeness, or usefulness of any information, apparatus, product, or process disclosed, or represents that its use would not infringe privately owned rights. Reference herein to any specific commercial product, process, or service by trade name, trademark, manufacturer, or otherwise does not necessarily constitute or imply its endorsement, recommendation, or favoring by the United States government or Lawrence Livermore National Security, LLC. The views and opinions of authors expressed herein do not necessarily state or reflect those of the United States government or Lawrence Livermore National Security, LLC, and shall not be used for advertising or product endorsement purposes.

1   **Assessing atmospheric stability and its impacts on rotor-disk wind characteristics at an**

2   **onshore wind farm**

3

4   Sonia Wharton[1] and Julie K. Lundquist[2,3]

5

6   [1]Atmospheric, Earth and Energy Division, Lawrence Livermore National Laboratory, P.O. Box

7   808, L-103, Livermore, CA 94551,

8   [2]Department of Atmospheric and Ocean Sciences, University of Colorado at Boulder, CUB-311,

9   Boulder, CO 80309,

10   [3]National Renewable Energy Laboratory, Golden, CO, 80401

12

13

14

15

16

17

19   **Abstract**

20   As the average hub height and blade diameter of new wind turbine installations continues

21   to increase, turbines typically encounter higher wind speeds, which enable them to extract large

22   amounts of energy, but they also face challenges due to the complex nature of wind flow and

23   turbulence in the planetary boundary layer (PBL). Wind speed and turbulence can vary greatly

24   across a turbine's rotor disk; this variability is partially due to whether the PBL is stable, neutral,

25   or convective. To assess the influence of stability on these wind characteristics, we utilize a

26   unique dataset including observations from two meteorological towers, a surface flux tower, and

27   high-resolution remote-sensing Sound Detection and Ranging (SODAR) instrument. We

28   compare several approaches to defining atmospheric stability to the Obukhov length (L). Typical

29   wind farm observations only allow for the calculation of a wind shear exponent (α) or horizontal

30   turbulence intensity (I_U) from cup anemometers, while SODAR gives measurements at multiple

31   heights in the rotor disk of turbulence intensity (I) in the latitudinal (I_u), longitudinal (I_v), and

32   vertical (I_w) directions and turbulence kinetic energy (TKE). Two methods for calculating

33   horizontal I from SODAR data are discussed. SODAR stability parameters are in high

34   agreement with the more physically-robust $L,$ with TKE exhibiting the best agreement, and show

35   promise for accurate characterizations of stability. Vertical profiles of wind speed and

36   turbulence, which likely affect turbine power performance, are highly correlated with stability

37   regime. At this wind farm, disregarding stability leads to over-assessments of the wind resource

38   during convective conditions and under-assessments during stable conditions.

39

40

41

Introduction

43   As utility-scale deployment of wind energy expands, turbine sizes and generating

44   capacities also are increasing. For example, more than 1,000 wind turbines currently in

45   operation in the U.S. have power producing capacities larger than 2 MW and new wind farms are

46   increasingly ordering turbines on the scale of 2.5 MW or greater. Furthermore, half of all newly

47   installed turbines in the U.S. in 2009 were at least 1.5 MW in capacity, with hub heights ranging

48   from 60 to 100 m above ground level (AGL) and rotor diameters on the order of 80 m [1].

49   Turbines with larger capacities generally utilize higher hub heights: the Enercon E-126 6 MW

50   turbine is designed for a hub height of 135 m, with a rotor disk of 126 m [2]. As turbines

51   penetrate higher altitudes, the area swept by the blades expands beyond the atmospheric surface

52   layer (~ the bottom 10% of the boundary layer, for e.g., if the depth of the boundary layer is

53   1000 m, the height of the surface layer is 100 m AGL) and into the convective mixed layer with

54   complex flows driven by buoyant turbulent mixing [3]. While mean wind velocity in the turbine

55   rotor disk (i.e., the blade swept area) largely determines the amount of power that is generated,

56   wind shear and turbulence intensity, which are measures of atmospheric stability, also appear to

57   play a role in power output [4-9]. Thus, defining parameters for atmospheric stability, including

58   accurate descriptions of how wind velocity and turbulence vary across the turbine rotor disk,

59   may prove beneficial to wind farm operations.

60   Stability in the lower boundary layer is largely driven by thermal gradients (called static

61   stability) and by frictional drag, either induced along the ground surface or from wind shear aloft

62   (called dynamic stability). For these reasons onshore wind farms generally experience strong

63   seasonal and diurnal patterns in the wind profile. Increased or decreased atmospheric mixing

64   causes wind velocity in the rotor disk to deviate from the traditionally expected profile whereby

65   pressure gradient forces cause wind speed to increase logarithmically with height from a

66   minimum found just above the ground surface to a maximum at the top of the boundary layer. In

67   fact, the logarithmic wind profile should be expected only when the boundary layer is near

68   neutral [10]. Near neutral conditions exist when wind speeds are very high, vertical gradients of

69   potential temperature are constant, and the buoyancy flux is nearly nonexistent. When turbulent

70   motions are enhanced, as during daylight hours when surface heating causes air to rise (positive

71   buoyancy), large-scale turbulent eddies reduce vertical gradients of temperature and velocity,

72   and wind speeds are nearly uniform with low shear throughout the rotor disk. Under stable

73   conditions, vertical motions are suppressed (negative buoyancy) and turbulence is dominated

74   either by mechanical forces near the surface (e.g. friction along the ground surface) or high wind

75   shear aloft (e.g. friction induced by a nocturnal low-level jet or gravity wave). A stable

76   boundary layer is characterized as having very little vertical mixing and strong gradients of

77   temperature and velocity. Generally at night, turbulent motions are subdued due to cooling at the

78   surface, the boundary layer is statically stable, and the air flow becomes stratified at heights

79   encountered by the wind turbine. This decoupling can lead to high shear conditions in the rotor

80   blade swept-area, with a shallow-depth acceleration of high-momentum air, between 100 and

81   300 m above the surface near the top of modern turbine rotors. Strong shear generated by these

82   jet profiles may generate turbulence aloft [11].

83   Stability classification schemes for the planetary boundary layer (PBL) are typically

84   based on vertical profiles of potential temperature θ ($\frac{\partial \theta}{\partial z} = \frac{\partial T}{\partial z} - \Gamma_d$, where Γ_d is the dry adiabatic

85   lapse rate (9.8 K/km)), the bulk Richardson number Ri (calculated from gradients of potential

86   temperature and wind speed) [12, 13], or the Obukhov length L (a surface layer scaling

87   parameter that is a function of surface heat and momentum fluxes) [14, 15]. Potential

88   temperature is useful in boundary layer studies because it normalizes the variations in

89   temperature in an air parcel due to changes in air pressure as it rises and descends. Vertical

90   profiles of potential temperature give the most straightforward indication of whether the

91   boundary layer is statically stable ($\frac{\partial \theta}{\partial z} > 0$), statically unstable ($\frac{\partial \theta}{\partial z} < 0$), or neutral ($\frac{\partial \theta}{\partial z} = 0$). A

92   complete temperature profile is, however, difficult to obtain because it requires either multiple

93   instruments on a very tall meteorological tower or a remote sensing platform equipped with a

94   temperature profiler, such as a Radio Acoustic Sounding System (RASS). Because these are

95   very expensive, boundary-layer studies instead often rely on the surface-based Obukhov length

96   to characterize stability, which requires a single sonic anemometer above the plant canopy or

97   bare ground, but this approach is not ideal for wind energy applications. L does not account for

98   low frequency, wave-dominated turbulence nor top-down forced boundary layers, such as those

99   that occur during stable conditions or on nights during a low-level jet (LLJ) [16], nor can it be

100   applied to heights above the surface layer [17, 18]. The Obukhov length is also problematic

101   during very stable conditions because surface fluxes may be small and intermittent [19] and thus

102   difficult to measure accurately. Therefore, a more universal, yet accurate stability parameter that

103   is based on available instrumentation is needed in the wind industry.

104   Wind farms typically have two means for inferring local stability, either from a

105   dimensionless wind shear exponent α, estimated from cup anemometers at least at two

106   measurement heights, or turbulence intensity I (the ratio of turbulence fluctuations to mean wind

107   speed), often from a single cup anemometer near hub height. High magnitudes of wind shear

108   suggest a stable boundary layer whereby the turbine blades are likely to encounter strongly

109   stratified flows across the rotor disk (e.g., much higher wind speeds at the top of the rotor than at

110   the bottom). Very high values of shear may cause out-of-plane bending loads on the blades and

111   damage turbine components. Low values of wind shear indicate convective or well-mixed

112   conditions across the rotor and a more uniform average velocity profile. Turbulence intensity is

113   also considered a means of quantifying atmospheric stability because a stable atmosphere is

114   generally characterized with low amounts of turbulence (except during a low-level jet or gravity

115   wave), while a convective atmosphere generally will be much more turbulent. High amounts of

116   intense and highly organized (coherent) turbulence are important to identify because they can

117   impose significant aerodynamic loads on the turbine and cause fatigue damage to the turbine

118   rotor [20, 21].

119   Previous investigations of the accuracy of turbine power curves have noted a dependency

120   of power performance on atmospheric stability through examination of the cup anemometer

121   stability parameters, α or I. Some stability studies have focused on specific stability-related

122   phenomena found in the lower boundary layer, including the nocturnal low-level jet which

123   produces a wind maxima [22-24] at heights near the top of the turbine rotor [25-28]. Other

124   researchers have focused on the sensitivity of power curves to the wind shear exponent [9, 29-

125   31] or to hub-height turbulence intensity [4, 8, 30, 32-34]. To our knowledge, this is the first

126   study to compare such a large set of independent stability parameters, including the Obukhov

127   length from sonic anemometry and high-resolution Sound Detection and Ranging (SODAR)

128   measurements of the wind shear exponent, turbulence intensity, and turbulence kinetic energy at

129   multiple heights spanning from the bottom to top of the rotor disk. We report high temporal and

130   spatial resolution measurements of wind speed, direction, and turbulence from multiple

131   instrument platforms, including SODAR, a pair of meteorological towers, and multiple turbines

132 over a full year. The dependence of turbine power generation on these stability parameters will

133 be addressed in a subsequent paper.

134

135 **Methods**

136 *Overview of site and available data*

137   The data in this study were collected at a wind farm located in western North America at

138 an elevation of near sea level, with some marine boundary layer influences. The area

139 experiences strong land-sea temperature differences, particularly during the summer months

140 when the land is much warmer than the coastal Pacific waters. The resulting pressure gradient

141 produces strong onshore winds consistently from a westerly or southwesterly direction. The site

142 has two distinct seasons: a wet, cool winter with frequent synoptic storms and a dry, warm

143 summer with little convective storm activity due to the presence of a semi-permanent high

144 pressure circulation over the Pacific Ocean. The landscape both upwind (called fetch) and at the

145 wind farm is grassland on rolling hills with elevation variations less than 100 m. Portions of the

146 site are used for grazing.

147   A number of horizontal-axis, three-bladed wind turbines, with rotor diameters of

148 approximately 80 m, are in operation at the wind farm, covering an area of approximately 6 km

149 by 10 km. The blades interact with the instantaneous wind speed in a disk-shaped area across

150 heights of 40 m to 120 m above the ground level (AGL), where 40 m is the minimum blade tip

151 height and 120 m is the maximum blade tip height. The nacelle and power generators are located

152 at 80 m AGL (referred to as hub-height). Each turbine has a heated cup anemometer (IceFree3,

153 NRG Systems, Hinesburg, VT, USA) located on the end of the nacelle, providing hub-height

154 estimates of wind speed. A subset of six leading-edge turbines was selected for analysis in this

155 study; these turbines are located in the northwestern region of the wind farm and are all upwind

156 of other turbines and obstacles.

157   The wind farm layout is shown in Figure 1 with the relative locations of the roving

158 SODAR platform, 50 m- and 80 m-tall meteorological towers, and subset of turbines used in this

159 analysis. The meteorological towers are located in the upwind portion of the wind farm and are

160 equipped with cup anemometers (#40, NRG Systems) at heights ranging from 30 m to 80 m

161 AGL. Additionally, wind direction, air temperature, and barometric pressure are measured near

162 the top of each tower. A Doppler mini SODAR (Model4000, Atmospheric Systems Corporation,

163 Santa Clarita, CA, USA) collected high vertical resolution, three-axis wind velocity data during

164 most of the year-long study in the northern region of the wind farm. SODAR data enabled the

165 calculations of a wind shear exponent, latitudinal, longitudinal, and vertical turbulence

166 intensities, and turbulence kinetic energy at 10 m intervals at heights representative of the rotor

167 disk, as discussed in detail below.

168   In addition, the Obukhov length was calculated from three-axis wind velocity and surface

169 heat flux measurements (WindMaster Pro 3-axis ultrasonic anemometer, Gill Instruments Ltd,

170 Hampshire, England) from an off-site research station approximately 15 km away in similar

171 terrain. All turbine and meteorological measurements except for the Obukhov length were

172 averaged over a 10-minute time period following IEC standards [35]. Measurements of wind

173 speed, momentum flux, and heat flux used in the Obukhov length were calculated from 30-

174 minute averages. Wind speed measurements were removed from the analysis when the

175 following criteria applied: standard deviation was less than 0.1 m/s, wind speed was greater than

176 25 m/s or less than 0.5 m/s, or wind flow was from an easterly direction and caused "tower

177 shadowing". Complete instrument details are listed in Table 1.

178   Throughout this paper, we define the wind velocities as the following: u and v are the

179   horizontal components of wind speed, where u is the mean wind speed in the latitudinal direction

180   (x) and v is the mean wind speed in the longitudinal direction (y), w is the mean wind speed in

181   the vertical direction (z), and u', v', and w' are perturbations of the instantaneous wind speed

182   components $u(t)$, $v(t)$, and $w(t)$ from the mean wind speeds u, v, and w, such that, $u' = u(t) - u$.

183   SODAR measures wind speed in three directions, while a cup anemometer gives only the

184   horizontal wind speed, U. SODAR U is calculated from the square root of the sum of latitudinal

185   and longitudinal velocities, such that, $U = \sqrt{u^2 + v^2}$. In this paper, nacelle wind speed refers to

186   the cup anemometer mounted on the nacelle hub at 80 m AGL while hub-height wind speed is

187   used in broader context to include all 80 m AGL wind speed measurements from either the

188   meteorological tower (cup anemometer), SODAR, or nacelle (cup anemometer). All analyses

189   were done using the statistical software package ORIGIN 8 (OriginLab Corp., Northampton,

190   MA, USA). We report the Pearson's correlation coefficient (r) and one-way ANOVA P-value

191   (P) at a significance level equal to the 95th confidence level ($P < 0.05$).

192

193   *Evaluation of power performance*

194   Power performance at an individual turbine was based on normalized power P_{norm} (%),

195     $$P_{norm} = \frac{P_{i,t}}{P_{i,rated}} \times 100 \qquad\qquad (1)$$

196   where $P_{i,t}$ is the average amount of power (kW) generated at turbine t over a 10 minute period

197   and P_{rated} is the maximum amount of power (kW) turbine t is potentially able to produce over a

198   ten minute period as determined by the manufacturer. A normalized power factor of 100%

9

199   indicates that a turbine is producing a power yield equal to the manufacturer's maximum power

200   rating (e.g., 2 MW for a 2 MW rated turbine). The manufacturer's power performance data

201   assumes standard atmospheric conditions including an assumption of neutral stability and

202   turbulence intensity between 10-15%. Air density corrections for the manufacturer power curves

203   using on-site air pressure and air temperature did not make a significant difference since this

204   wind farm is at near sea level. Normalized power was calculated for each turbine in the subset

205   every 10 minutes during the study period. We used leading-edge turbines to remove any effects

206   that turbine-induced wakes may have on turbine power performance. Also, the distance between

207   any upwind obstacles (e.g., a meteorological tower) and a downwind turbine was checked to

208   verify that the turbine was no closer than four times the rotor diameter from the upwind obstacle

209   [35].

210

211   *Meteorological measurements and stability parameters*

212   Vertical profiles of mean horizontal wind speed (U) (m s^{-1}) and turbulent fluctuations in

213   the horizontal wind speed (σ_U) (m s^{-1}) were available from cup anemometers on two

214   meteorological towers (50 m and 80 m tall). Three cup anemometers were mounted on the 50 m

215   tower at heights of 30 m, 40 m, and 50 m AGL. The 80 m tower was equipped with three cup

216   anemometers at heights equal to 50 m, 60 m, and 80 m AGL. The cup anemometers measured

217   horizontal wind speed at a sampling rate of 1 Hz with an accuracy of 0.3 m s^{-1}. Wind direction,

218   barometric pressure, and air temperature (T_a) were measured at 47 m AGL on the 50 m tall tower

219   and at 77 m AGL on the 80 m tall tower. Frequent data outages in T_a, as well as the 8 km

220 distance between the two meteorological towers, prevented the calculation of a vertical potential

221 temperature profile to determine atmospheric stability at this site.

222   SODAR measurements of latitudinal, longitudinal, and vertical wind speed (u, v, w) (m s⁻

223 ¹), wind direction, and turbulent velocity fluctuations (σ_u, σ_v, σ_w) (m s⁻¹) were available during the

224 majority of the study period. The SODAR transmits three high frequency (4500 Hz) acoustic

225 beams at a pulse width of 60 ms, and u, v, and w are calculated by analyzing the frequency shift

226 in spectral energy in the return signal from each beam [36, 37]. The wind vectors were measured

227 at 10 m intervals from 20 m to 200 m, for a total of 19 different height measurements above the

228 ground surface, with an accuracy of 0.5 m s⁻¹. Wind speed and direction were averaged over 10-

229 minute intervals. The raw data were quality-controlled according to accepted SODAR standards,

230 e.g. [38]. 10-minute periods that failed to meet thresholds for percentage of acceptable data (>

231 15% bad data) and signal-to-noise ratio (SNR < 7) were removed. The system operated from

232 July 2007 to May 2008 with major outages in the rainy season (November, December and

233 January). On average, daytime (nighttime) SODAR data recovery was greater than 95% (90%)

234 at 40 m, 90% (85%) at 80 m, and 75% (83%) at 120 m AGL. The SODAR was not stationary

235 during the study period and was moved to three site locations (SODAR1, SODAR2, and

236 SODAR3) within an area of 4.8 km by 1.5 km during the periods: July 2007 to mid-August

237 2007, mid-August 2007 to September 2007, and October 2007 to May 2008. These times

238 correspond to SODAR1, SODAR2 and SODAR3 in Figure 1, respectively.

239   SODAR and cup anemometer wind velocities were used to calculate a dimensionless

240 wind shear exponent α using the power law expression [39],

241 $$U(z) = U_R \left(\frac{z}{z_R}\right)^\alpha \tag{2}$$

242 where U is the mean horizontal wind speed (m s^{-1}) at height z (m) and U_R is the mean horizontal

243 wind speed (m s^{-1}) at a reference height z_R (m); by convention, height z_R is closer to the ground

244 than z. A wind shear exponent is traditionally used to estimate variations in available wind

245 power by height, when direct measurements of wind speed across the rotor and stability are

246 unavailable [40]. Here, three wind shear exponents were calculated using SODAR wind speed

247 measurements at 40, 80, and 120 m: α_{40_120} parameterizes stability across the entire rotor disk,

248 α_{40_80} parameterizes stability across the lower half of the rotor disk, and α_{80_120} parameterizes

249 stability across the upper half of the rotor disk. A fourth, α, α_{50_80}, was calculated using the 50

250 and 80 m meteorological tower cup anemometer data for comparison to the SODAR shear

251 exponent α_{40_80}. Only the time periods when the wind speed was greater than the turbine cut-in

252 speed were used to calculate α.

253   The wind shear exponent describes the degree of atmospheric stability based on the

254 presence (shear or no shear) and amount (low or high shear) of stratified flow but is not a direct

255 measure of stability. Historically, a constant α-value of 1/7 (0.14) has been used to extrapolate

256 the wind speed taken at a reference height (usually from the nacelle anemometer) to all other

257 heights within the blade-swept area when the wind profile is unknown. The one-seventh

258 constant has been attributed by [41] to von Karman's work indicating a correspondence between

259 wind flow in the surface layer and experimental flow over flat plates and to observations taken in

260 the boundary layer in the 1920's by [42]. A few studies recognized early on that serious errors

261 can be introduced by reliance on the power law, Eq (2), to estimate the wind speed profile in

262 wind power applications [43-45]. First, the power law has no theoretical basis for extrapolating

263 wind speed within the boundary layer because it is not based on the basic principles of fluid

264 mechanics and is instead derived empirically. Second, the power law should only be considered

12

265   valid during neutral conditions in homogeneous, flat terrain. Finally, the power law does not

266   acknowledge the possibility of variable wind shear across the rotor disk and its impact on

267   turbulence.

268   In contrast to the wind shear exponent, which measures the amount of wind shear that

269   may produce turbulence, turbulence intensity I (%) uses measurements of velocity fluctuations in

270   the boundary layer to characterize stability and is a statistical descriptor of the overall level of

271   turbulence in relation to mean wind speed. High I magnitudes indicate that a significant portion

272   of wind energy is composed of turbulent flow, while low I values indicate laminar flow with less

273   turbulence. Three component turbulence intensities can be calculated when u, v, and w

274   observations are available, as from a SODAR or sonic anemometer. These include I_u, the

275   latitudinal turbulence intensity, I_v, the longitudinal turbulence intensity, and I_w, the vertical

276   turbulence intensity. The first turbulence intensity, I_u, describes the relative amount of

277   turbulence in the x direction in relation to the mean horizontal wind speed, following [46],

278            $$I_u = \frac{\sigma_u}{U}$$ (3)

279   where σ_u (m s^{-1}) is the average standard deviation of the latitudinal velocities over a 10-minute

280   period. Likewise turbulence intensity in the longitudinal direction is,

281            $$I_v = \frac{\sigma_v}{U}$$ (4)

282
       and turbulence intensity in the vertical direction is,

283            $$I_w = \frac{\sigma_w}{U}$$ (5)

284   Note that calculations of longitudinal I_v or vertical I_w are not possible with a cup

285   anemometer since the instrument measures only horizontal wind speed (U), and not the

286   components u, v, and w. We assumed here that the cup anemometer is insensitive to any changes

287   in the vertical velocity. For the cup anemometers, turbulence intensity was determined by

288   calculating a horizontal turbulence intensity,

289            $$I_{Ucup} = \frac{\sigma_U}{U}$$ (6)

290   SODAR I magnitudes are not directly comparable to those from the cup anemometer because the

291   expressions for I in Eqs (3-5) are not equal to I in Eq (6). In order to directly compare the

292   instruments, we calculated two alternative expressions for horizontal turbulence intensity from

293   the SODAR to include the standard deviations of u and v. Eq (7) appears to be the more

294   accepted way to calculate SODAR I_U in the wind industry, whereby I_U is the average of the

295   latitudinal and longitudinal turbulence fluctuations and assumes that turbulence is isotropic,

296            $$I_{U1SODAR} = \frac{\sum_{i=u,v} \sigma_i}{2U}$$ (7)

297

In Eq (8), we followed methodology adopted by micrometeorologists and calculated a horizontal

298

turbulence intensity which uses the square-root of the sum of turbulence in the horizontal wind

299

components and makes no assumptions about the isotropic nature of turbulence,

300            $$I_{U2SODAR} = \frac{\sqrt{(\sigma_u^2 + \sigma_v^2)}}{U}$$ (8)

301 The expression for turbulence intensity in Eq (8) is found in [47] and is similar to derivations

302 found in [46, 48]. Note that Eq (7) (the "averaging method") and Eq (8) (the "square-root

303 method) will not give identical magnitudes of I_U, even if turbulence is isotropic and σ_u equals σ_v

304 because the two expressions for horizontal turbulence are not equal.

305   SODAR turbulence intensities were calculated at 10-minute intervals at each of the nine

306 measurement heights in the rotor disk. Cup anemometer I was calculated for each 10-minute

307 period at heights of 50 and 80 m using the meteorological tower cup anemometer measurements.

308 Only the time periods when U was greater than the turbine cut-in speed and the standard

309 deviations were greater than 0.1 m s^{-1} were included. These criteria excluded extremely high

310 turbulence intensities caused by the presence of very low wind speeds and very low turbulence

311 intensities caused by unrealistically low variance.

312   Related to SODAR I, turbulence kinetic energy TKE (m^2 s^{-2}) was calculated from

313 SODAR data using the three turbulence components as in Eq (9),

314
$$TKE = \frac{1}{2}(\sigma_u^2 + \sigma_v^2 + \sigma_w^2) \tag{9}$$

315 *TKE* is a measure of the intensity of turbulence and is directly related to the transport of

316 momentum (shear-generated turbulence that is strongest in the horizontal direction) and heat

317 (thermal-generated turbulence in the vertical direction) through the boundary layer. Hence, *TKE*

318 is the sum of all measurable sources of turbulence, both convective and mechanically-generated.

319 Here, *TKE* was calculated for each of the 19 SODAR measurement heights (20-200 m AGL).

320   *TKE* varies with height. For example, in an unstable boundary layer, *TKE* generally

321 increases with height until a maximum is found at the level where free convection dominates.

322 When strong winds are present or during neutral conditions, *TKE* may be nearly constant or

323 decrease slightly with height [17]. During stable nighttime conditions, *TKE* often decreases

324 rapidly with height from a maximum value found just above the surface. An exception to this

325 occurs when low-level jets or other elevated sources of turbulence such as breaking gravity

326 waves are present. If nighttime *TKE* is generated at levels above the surface in a statically stable

327 atmosphere and is transported downward, then this behavior suggests the presence of high wind

328 shear and a LLJ [16, 49-51]. During a LLJ, very high wind speeds may be found at heights equal

329 to the top of turbine rotors (~100-150 m AGL) [52], but the potential for high power generation

330 can be offset by the potential for structural turbine damage caused by intense, coherent

331 turbulence structures just below the LLJ [21].

332 Finally, a nearby university research station provided 3-axis wind velocity and sensible

333 heat flux data from a sonic anemometer and a fast-response thermocouple during the study

334 period to calculate the stability length scale L (Obukhov length). The research station has some

335 localized differences compared to the wind farm, including a fetch with flatter terrain and a

336 slightly lower estimate of aerodynamic roughness length, but the winds are consistently from the

337 same direction. Using a fast-response (output rate of 20 Hz), multi-axis sonic anemometer,

338 measurements of mean latitudinal, longitudinal, and vertical wind speed, as well as fluctuations

339 from the mean (u', v' and w'), offered detailed information about the structures of organized

340 turbulence. The Obukhov length (L) (m) was used as a scaling parameter to indicate atmospheric

341 mixing conditions in the surface layer following Monin-Obukhov similarity theory [17, 53-55],

342
$$L = -\frac{\theta_v \cdot u_*^3}{k \cdot g \cdot \overline{w'\theta_v'}}$$
(10)

343   where θ_v is the virtual potential temperature (K), k is the von Karman constant (0.4), g is

344   acceleration due to gravity (9.8 m s^{-2}), $\overline{w'\theta'_v}$ is the kinematic sensible heat flux (W m^{-2}), and

345   friction velocity, u_* (m s^{-1}) is defined from the kinematic momentum fluxes, where u_*

346     $= (\overline{u'v'}^2 + \overline{v'w'}^2)^{1/4}$. Calculation of potential virtual temperature (θ_v) in the sensible heat flux

347   eliminates the "apparent" temperature variations from changes in air pressure of an air parcel as

348   it rises and descends. The sign of the kinematic sensible heat flux in Eq (10) indicates whether

349   the boundary layer is statically stable ($\overline{w'\theta'_v} < 0$) or statically unstable ($\overline{w'\theta'_v} > 0$). A physical

350   interpretation of the Obukhov length is that the absolute value of L is proportional to the height

351   (in meters) above the surface at which thermal-produced turbulence replaces shear as the

352   dominant influence over turbulence. In contrast to the wind shear exponent, L is valid in

353   moderately unstable or stable conditions as well as neutral boundary layers.

354   Eq (10) can be expressed as a non-dimensional scaling parameter z/L, where z is the

355   height of the sonic anemometer ($z = 3.2$ m). Normalizing L by the measurement height is often

356   done in boundary layer studies because L magnitudes are extremely non-linear. Most of the

357   figures in this paper use z/L to take advantage of its linearity although the stability thresholds in

358   Table 2 are given for L to enable direct comparisons with other studies in the literature. L or z/L

359   is defined as a negative quantity under convective or statically unstable conditions (the heat flux

360   is directed away from the surface) and a positive quantity under statically stable conditions (the

361   heat flux is directed towards the surface). L approaches infinity ($z/L \sim 0$) under neutral

362   conditions.

363   *Stability classifications*

364   For each 10-minute averaging period, we described the boundary layer stability

365   conditions based on Obukhov length L, wind shear exponent α (at various heights in the rotor

366   disk), turbulence intensity I (at 80 m AGL), and turbulence kinetic energy TKE (at 80 m AGL).

367   We classified each 10-minute period as belonging to one of five stability classes: strongly stable,

368   stable, neutral (includes slightly stable and slightly convective), convective, or strongly

369   convective. The stability thresholds, listed in Table 2, were based largely on published values,

370   although the criteria have been modified slightly according to the range of atmospheric

371   conditions and terrain observed at this wind farm.

372   The Obukhov length thresholds were based on stability classifications given by [12, 17],

373   and are similar to those used by [56] in a study of offshore wind profiles and [57] in their

374   assessment of turbine damage induced by atmospheric stability effects. Note that our threshold

375   for neutral conditions is less conservative than found in [56-57] and includes the stability classes

376   weakly stable and weakly convective. The wind shear exponent thresholds were based on work

377   by [8, 19, 58], although we defined a slightly lower threshold for strongly stable conditions ($\alpha >$

378   0.3). Less information is available for TKE stability criteria in wind power applications and this

379   paper appears to be one of the first applications of TKE in wind energy stability studies. Our

380   *TKE* thresholds were based on boundary layer field campaign data found in [17].

381   Because turbulence intensity is a relative quantity, I thresholds appear to be very sensitive

382   to the type of instrument and methodology used. The thresholds for cup anemometer I are

383   similar to those found in [4, 30, 32, 59], although we defined more detailed stability classes. For

384   example, [30] define just two stability classes based on a low turbulence threshold ($I_U = 5$ to

385   11%) and a high turbulence threshold ($I_U = 11$ to 17%). We defined five I_U stability classes

386   including one that describes a near neutral atmosphere using intermediate values of turbulence

387   intensity. Similar to our site, [4] at a West Coast wind farm defines the following I_U thresholds,

388   from low turbulence to high turbulence as: 0 to 5%, 5 to 10%, 10 to 15%, and 15 to 30%.

389   Magnitudes of SODAR-based horizontal turbulence intensity depended on the

390   methodology chosen to calculate turbulence in the horizontal direction. When the average of σ_u

391   and σ_v was used to calculate σ_U, as in Eq (7), we found stability thresholds for $I_{U1SODAR}$ similar to

392   the cup anemometer I_U, although cup anemometers are known to underestimate turbulence [60].

393   This difference is discussed later. In contrast, the turbulence intensity magnitudes were greater

394   when σ_U was calculated using the square-root of the sum of σ^2_u and σ^2_v (Eq 8), and our stability

395   criteria for $I_{U2SODAR}$ reflect this offset. We included $I_{U2SODAR}$ in this analysis because, from a

396   micrometeorological perspective, we believe that it is the best representation of the "actual"

397   amount of turbulence present in the horizontal direction.

398

399   **Results**

400   *Seasonal power, wind speed and direction*

401   This wind farm experiences two distinct wind power seasons: autumn/winter and

402   spring/summer, as determined by the regional climatology. The autumn/winter months are

403   dominated by synoptic-scale circulations while the warm season is dominated by diurnal sea-

404   breeze circulations in response to thermal forcing. The rainy, winter season consisted of months

405   with lower nacelle wind speeds and lower power outputs than average. Greater power

406   production occurred during the warm season coinciding with faster nacelle winds speeds. Figure

407   2 shows seasonal average normalized power (a) and nacelle wind speed (b) for a single turbine,

408   Turbine #1. Average normalized power (nacelle wind speed) was 22% (4.89 m s^{-1}) in winter,

409   53% (8.12 m s^{-1}) in spring, 58% (8.38 m s^{-1}) in summer, and 23% (5.11 m s^{-1}) in autumn. Power

410   and wind speed conditions observed at Turbine #1 were representative of the entire turbine

411   subset during the year. Annual average normalized power was 40% for all six turbines in

412   comparison to 39% at Turbine #1.

413   Mean diurnal P_{norm} values are shown in Figure 3 for Turbine #1. More power was

414   generated at night than during the day, although diurnal variability varied greatly by season. The

415   largest diurnal range in normalized power ($\Delta P_{norm} \sim 45\%$) was observed in the summer while

416   diurnal variability was minimal ($\Delta P_{norm} < 15\%$) in winter and autumn and moderate ($\Delta P_{norm} \sim$

417   25%) in the spring. Average nighttime (22:00 – 2:00 Pacific Standard Time) normalized power

418   was 23% in winter, 63% in spring, 77% in summer, and 26% in autumn. Average midday (10:00

419   – 14:00 Pacific Standard Time) normalized power was 16% in winter, 40% in spring, 32% in

420   summer, and 14% in autumn. Peak power output was observed around midnight in the summer

421   and average P_{norm} reached 80%.

422   Figure 4 compares seasonal wind speed observations at 40, 80, and 120 m from the

423   SODAR (a) and meteorological tower cup anemometers (b). Note that the highest measurement

424   height on the meteorological tower is only 80 m. Similar to the nacelle wind speeds (Figure 3),

425   SODAR and meteorological tower wind speeds were higher at night than during the day and

426   higher during the warm season than in the cool season. The largest seasonal variability in wind

427   speed occurred during the nighttime hours; for example, mean winter 80 m U was 5.4 m s^{-1} while

428   mean summer 80 m U was nearly double, 10.1 m s^{-1}. Less seasonal variability was present

429   during the daylight hours, although daytime wind speeds also seasonally peaked during the

430   summer months. Although nighttime wind shear was commonly observed throughout the year, it

431   was most prevalent during the summer months, as evident in the high-resolution SODAR data.

432   SODAR wind speed differences approached 4 m s^{-1} between 40 m and 120 m on summer nights

433   (Figure 4a). Observations of wind shear at the meteorological tower (Figure 4b) were slightly

434   less than wind shear measured by the SODAR. For example, average 40 m-to-80 m wind shear

435   was 1.4 m s^{-1} at the meteorological tower in comparison to 2.0 m s^{-1} from the SODAR on

436   summer nights. Unlike SODAR, the meteorological tower cup anemometers also indicated a

437   prevalence of negative, daytime wind shear (faster wind speeds at 40 m than 80 m) during spring

438   and summer. An explanation for this is discussed next.

439   Over the study period, the SODAR and cup anemometers measured slight differences in

440   mean wind speed. For example, annual mean nighttime U (80 m) was 8.5 ± 2.8 m s^{-1} from

441   SODAR (Figure 4a) and 8.3 ± 2.6 m s^{-1} from the meteorological tower cup anemometer (Figure

442   4b). Annual mean daytime U (80 m) was 6.5 ± 3.2 m s^{-1} from SODAR and 6.7 ± 3.0 m s^{-1} from

443   the meteorological tower. The Pearson's correlation coefficient (r) between the SODAR and

444   meteorological tower 80 m wind speeds was r = 0.87 during the day and r = 0.69 at night during

445   the spring and summer months. The meteorological tower showed greater variability in the

446   daytime wind speeds than the SODAR between heights of 40 m and 80 m. This may be an

447   artifact of the 8 km distance between the two meteorological towers because U at 40 m

448   (measured at the 50 m tower) was on average higher than U at 80 m (measured at the 80 m

449   tower) which resulted in average negative wind shear as seen in Figure 4b. The meteorological

450   towers and SODAR also were not co-located and were separated by a distance of 5 km between

451   the 80 m tall tower and SODAR and nearly 6 km between the 50 m tower and farthest located

452   SODAR position. These distances, across mildly hilly terrain, explain some of the discrepancy

453   between the wind speed measurements.

454   The predominant wind direction at the wind farm was from the west-southwest from

455   March through October while a bimodal wind direction distribution was observed from

456   November-February with a primary peak in the west-southwest direction and a secondary peak

457   in north-northeast. Wind direction histograms for two months, February and July, are shown in

458   Figure 5 for three SODAR heights (40, 80, and 120 m) and are separated into nighttime and

459   daytime periods to show both seasonal and temporal distributions. 80 m (hub-height) winds

460   were from the west-southwest over 85% of the time on July nights (Figure 5e) in contrast to 55%

461   of the time on February nights (Figure 5b). During the daylight hours, 80 m winds were from the

462   west-southwest 62% of the time in July while only 38% of the time in February. Overall,

463   directional shear (change in wind direction with height) across heights representing the rotor disk

464   was negligible, although greater shear was observed in February than in July. In contrast to wind

465   speed in Figure 4, wind direction at the wind farm indicated only a small degree of temporal

466   (night versus day) and spatial (vertical height and instrument location) variability during the peak

467   power production summer months (Figure 5d-f).

468

469   *Stability parameter analysis and comparison*

470   Due to less data recovery in the rainy autumn/winter months and the occurrence of peak

471   power production in the spring and summer months, all subsequent analysis concentrates on the

472   warm season only. The percentage of summertime periods defined as stable (includes moderate

473   and strong), neutral (includes weakly stable and weakly convective), or convective (includes

474   moderate and strong) by the Obukhov length, wind shear exponent (across 40 to 120 m),

475   horizontal turbulence intensity (at 80 m), and turbulence kinetic energy (at 80 m) are shown in

476   Figure 6. The Obukhov length indicated stable:neutral:convective conditions in a 42:18:40 ratio

477 with weakly stable and weakly convective regimes included in the neutral category (Figure 6a).

478 As expected, daytime periods were primarily classified as strongly convective, convective or

479 weakly convective, while nighttime periods were strongly stable, stable, or slightly stable.

480 Stable or very stable conditions were present on nearly every nighttime hour during the spring

481 and summer months. The stability parameters, α_{40_120} (6b), $I_{U2SODAR}$ (6e), and TKE (6f) showed

482 highest agreement with L and predicted stable:neutral:convective ratios of 42:22:36, 40:20:40,

483 and 42:20:38, respectively, while I_{Ucup} (6c) and $I_{U1SODAR}$ (6d) under-predicted convective

484 conditions by more than 10%.

485   Box-plot histograms of 10-minute α (40 to 120 m), SODAR I_{U2} (80 m), and TKE (80 m)

486 magnitudes according to z/L stability class are shown in Figure 7. The box plots show the mean,

487 median, 25th and 75th percentiles for each stability parameter after bin-averaging by z/L. Overall

488 there was high agreement between the derived stability parameters and the normalized Obukhov

489 length. For example, when z/L indicated neutral conditions ($z/L \approx 0$), the median (25th

490 percentile) (75th percentile) value for α_{40_120} was 0.14 (0.06) (0.23), $I_{U2SODAR}$ was 12.0% (9.7)

491 (13.8), and TKE was 0.76 m^2 s^{-2} (0.54) (1.00). When z/L indicated stable conditions ($z/L > 0$),

492 the median (25th percentile) (75th percentile) α_{40_120} = 0.31 (0.24) (0.36), $I_{U2SODAR}$ = 8.2% (7.3)

493 (9.1), and TKE = 0.42 m^2 s^{-2} (0.31) (0.55). When z/L indicated convective conditions ($z/L < 0$),

494 the median (25th percentile) (75th percentile) α_{40_120} = 0.02 (-0.04) (0.07), $I_{U2SODAR}$ = 24.2% (17.2)

495 (33.4), and TKE = 1.20 m^2 s^{-2} (0.98) (1.38). The median values for α_{40_120}, $I_{U2SODAR}$, and TKE are

496 well within the thresholds given in Table 2 for the three major stability regimes (stable, neutral,

497 and convective). Most of the 25th and 75th percentiles are also within the thresholds.

498   Mean diurnal patterns for the stability parameters during spring and summer are shown in

499 Figure 8. In each panel, the gray shading indicates stable conditions, the x-notched shading is

23

500   neutral conditions, and the white shading is convective conditions. Almost all of the stability

501   parameters show distinctly stable conditions at the night and convective conditions during the

502   day. The normalized Obukhov length is shown for comparison to the on-site, derived stability

503   parameters and shows that on average stable conditions existed from 19:00-5:00 Pacific Standard

504   Time, neutral conditions occurred around sunrise and sunset, and convective conditions were

505   between 8:00-16:00 Pacific Standard Time (Figure 8a). Figure 8b shows the three SODAR wind

506   shear exponents: α_{40_120} (shear across the entire rotor disk), α_{40_80} (shear across the lower half),

507   and α_{80_120} (shear across the upper half), in comparison to the meteorological tower wind shear

508   exponent, α_{50_80} (shear across the lower half). Diurnal wind shear variability was large and all

509   four wind shear exponents were, on average, greater than 0.2 at night (indicating high shear and

510   stable conditions) and less than 0.1 during the day (indicating low shear and convective

511   conditions). Very high shear conditions ($\alpha = 0.3$ to 0.4) were consistently observed on spring

512   and summer nights in the upper half of the rotor disk, possibly indicating the presence of low-

513   level jet structures at heights above the top blade tip, which did not penetrate to the lower half of

514   the rotor. During the day, wind shear was generally highest in the lower half of the rotor disk

515   (40 m to 80 m) while α_{40_120} values indicated a well-mixed boundary layer across the entire swept

516   area. Generally, magnitudes of SODAR α_{40_80} and cup anemometer α_{50_80} were very similar, as

517   expected, although the cup anemometer indicated slightly less wind shear during the daylight

518   hours.

519   Diurnal magnitudes of I_U indicated systematic instrument differences between the cup

520   anemometer and SODAR as well as differences in the methodology used to calculate SODAR

521   horizontal turbulence. I_{Ucup} indicated, on average, higher turbulence intensities closer to the

522   ground (50 m versus 80 m) during both nighttime and daytime hours (Figure 8c). Mean cup

24

523   anemometer I_U was 13.5% at 50 m and 12.7% at 80 m during midday hours and 9.7% at 50 m

524   and 7.9% at 80 m at night. I_{U_50} and I_{U_80} were measured at different locations in the wind farm

525   and are thus not directly comparable. The first SODAR-derived horizontal turbulence intensity,

526    $I_{U1SODAR}$, showed a similar amount of diurnal variability as I_{Ucup}, although the SODAR parameter

527   shows highest daytime I magnitudes at 120 m and highest nighttime I values at 40 m. Mean

528   nighttime 40 m (80 m) (120 m) $I_{U1SODAR}$ was 7.6% (6.2%) (5.5%). Mean daytime 40 m (80 m)

529   (120 m) $I_{U1SODAR}$ was 13.5% (14.4%) (14.8%). These differences with height and time of day are

530   realistic given that turbulence at night is shear-driven (e.g., friction along the surface), while

531   daytime turbulence is dominated by large, buoyant eddies.

532   The second SODAR-derived I parameter, $I_{U2SODAR}$, showed a greater amount of diurnal

533   variability than either I_{Ucup} or $I_{U1SODAR}$ and is shown in Figure 8e. Hub-height $I_{U2SODAR}$ ranged

534   from 20.3% during midday to 8.6% at night. $I_{U2SODAR}$ also showed slightly more stratification

535   with height during the nighttime hours: mean I =10.8% at 40 m and 7.7% at 120 m. The largest

536   difference between hub-height I_{Ucup}, $I_{U1SODAR}$, and $I_{U2SODAR}$ magnitudes occurred during the

537   daylight hours and peak midday values ranged from 14.2% (I_{Ucup}) to 21.7% ($I_{U2SODAR}$). The cup

538   anemometers systematically measured smaller turbulence intensities during the daylight hours as

539   compared to SODAR. Further analysis showed that the instrument differences came largely

540   from differences in the 10-minute standard deviations (σ_U). Cup anemometer σ_U magnitudes

541   were generally lower than both methods used to calculate SODAR σ_U. The "square-root"

542   method (Eq 8) yielded up to 5% higher I_U magnitudes during the day than did the "averaging

543   method" (Eq 7). A larger range of magnitudes made it possible to use $I_{U2SODAR}$ to distinguish

544   very convective conditions from moderately convective.

545   The mean diurnal pattern for turbulence kinetic energy at heights of 40, 80, and 120 m

546 appears in Figure 8f. The degree of diurnal variability in *TKE* is very similar to that observed for

547 $I_{U2SODAR}$. As with the SODAR *I* parameters, nighttime *TKE* decreased with height, while

548 daytime *TKE* increased with height. Mean daytime (nighttime) *TKE* magnitudes were 1.60 m^2 s$^-$

549 ^{2} (0.63 m^2 s^{-2}) at 120 m, 1.58 m^2 s^{-2} (0.64 m^2 s^{-2}) at 80 m, and 1.42 m^2 s^{-2} (0.71 m^2 s^{-2}) at 40 m.

550 As expected, nighttime *TKE* magnitudes were indicative of stable, stratified flows, while daytime

551 *TKE* showed a much more turbulent atmosphere.

552

553 *Stability influence on wind velocity and turbulence profiles*

554   The following sections use $I_{U2SODAR}$ (at 80 m) to quantify the effects of atmospheric

555 stability on the rotor disk wind speed and turbulence profiles during spring and summer. 10-

556 minute wind speeds at 40, 80, and 120 m were averaged by stability class in Figure 9 and are

557 compared against seasonal averages. Stability-correlated variability was particularly high during

558 the spring and summer months. Hub height wind speed was significantly lower ($P < 0.05$)

559 during convective or strongly convective conditions than during strongly stable, stable, or neutral

560 regimes. As expected, convective conditions showed almost no wind speed variability with

561 height, while wind speeds were highly stratified across the rotor during stable and very stable

562 conditions. Maximum wind speeds were observed during stable conditions, at all heights, with

563 the largest stability-related differences occurring at the top of the rotor during the summer. For

564 example, summer-time mean 120 m wind speed was 14.0 m s^{-1} during very stable conditions in

565 comparison to 3.0 m s^{-1} during very convective conditions (Figure 9b).

566   Vertical profiles of wind speed and *TKE* at all heights across the rotor disk are shown in

567   Figures 10 (for spring) and 11 (for summer) and are segregated according to stability class.

568   Using wind speed observations at 80 m, and assuming an α value of 1/7 in Equation (2), the

569   power law wind speed profile was also calculated. These figures show clear distinctions in how

570   measured wind speed varies with height depending on atmospheric stability. Additionally, it is

571   clear that a constant wind shear exponent is not sufficient in predicting the mean wind speed

572   profile under non-neutral conditions.

573   In Figure 10a, the power law inaccurately predicted wind speeds at the top and bottom of

574   the rotor disk during both stable and convective conditions. For example, during stable

575   conditions, the power law expression underestimated wind speed in the upper half of the rotor by

576   1 to 1.5 m s^{-1} and overestimated wind speed in the lower half by 0.5 to 1 m s^{-1}. While during

577   convective conditions, the power law overestimated wind speed in the upper half of the rotor by

578   1.0 to 1.5 m s^{-1}, and underestimated wind speed in the lower half by 0.3 m s^{-1}. In Figure 10b,

579   SODAR observations show that *TKE* decreased with height (up to 100 m) during stable

580   conditions, was nearly constant with height during near-neutral conditions, and increased rapidly

581   with height during convective conditions. The largest changes in *TKE* with height were

582   observed in the lower half of the rotor, regardless of stability regime. A significant peak in *TKE*

583   below the wind speed maxima (~ 130-150 m) was not noticeable during very stable conditions.

584   Summertime SODAR profiles of wind speed were similar to those observed in the spring,

585   except that even stronger stability influences were observed during strongly stable and strongly

586   convective conditions (Figure 11a). During strongly stable conditions, wind speed at the top of

587   the rotor approached 14 m s^{-1}. This velocity was 1.5 m s^{-1} greater than the predicted wind speed

588   at this height (using $\alpha = 1/7$), while in the lower half of the rotor, U was 10 m s^{-1}, a full meter per

589 second slower than predicted with the power law. In contrast, during strongly convective

590 conditions, the power law overestimated U in the top half of the rotor by 1.5 to 2.0 m s^{-1} and

591 underestimated U in the lower half by 0.5 m s^{-1}. *TKE* profiles during the summer season are

592 shown in Figure 11b. Sharp increases in *TKE* with height were observed during convective

593 conditions, while *TKE* was nearly constant with height during neutral and stable conditions. A

594 slight peak in *TKE* was visible during very stable conditions at 140 m which may indicate the

595 presence of low-level jets on summer nights (a wind maxima is also present at 150 m), although

596 confirmation of LLJs is not possible without further investigation.

597

598 **Discussion**

599   With the rapid expansion of wind farms and the significant penetration of wind energy

600 into power markets, accurate estimates of wind power availability and the dependence of the

601 wind resource on atmospheric boundary layer conditions, including stability, are required to

602 assess wind plant performance. In this study, a unique dataset from an onshore wind farm was

603 explored to quantify the utility of various parameters of atmospheric stability, as well as

604 document the impact of atmospheric stability on profiles of wind speed and turbulence across the

605 rotor disk. In addition to typical wind farm meteorological tower and nacelle cup anemometers,

606 this extensive dataset included measurements from a remote-sensing SODAR and an offsite

607 three-dimensional sonic anemometer.

608   On average, wind farms in the contiguous U.S. produce maximum power in January and

609 minimum power in August [61]. In contrast, this wind farm exhibited maximum power output

610 during the warmer months, with peak power produced on strongly stable spring and summer

611 nights. The power season was largely driven by regional climatology. The climate includes a

612   dry, warm season with strong thermal gradients and strong onshore flow, and a wet, cool season

613   dominated by synoptic storms. The summertime peak in power coincided with higher wind

614   speeds in the rotor disk, and in particular, with maximum wind speeds found at the top of the

615   rotor (100 to 120 m) during stable nighttime conditions. The wintertime drop in power was due

616   to fewer occurrences of strong, stable nighttime flows and an overall decrease in wind speeds at

617   all heights within the rotor disk.

618   The on-site stability parameters α_{120_40}, $I_{U2SODAR,}$ and TKE compared well with the sonic

619   anemometer measurement of stability, L, while I_{Ucup} and $I_{U1SODAR}$ tended to under-predicted

620   convective conditions. Previous wind farm studies have determined stability based on one or

621   two of these parameters [5, 8], while ours is the first study of our knowledge to compare such a

622   large set of independent stability parameters. Observations of 3-directional turbulence were

623   available on-site only because of the presence of the SODAR, although deployment of 3-D sonic

624   anemometers on a tall meteorological tower could also enable quantification of TKE profiles.

625   Along with power production and mean wind speed, stability regimes at our site were highly

626   seasonal. The largest contrasts between stable and convective conditions appeared during

627   thermally-driven onshore flow in the spring and summer months.

628   We observed high amounts of wind shear across the rotor disk on summer nights in

629   agreement with values found in other studies [30, 62] indicating that the turbines at our site are,

630   at times, above the atmospheric surface layer and are encountering complex, decoupled flow.

631   Although all of the wind shear exponents characterized stability in agreement with L, we found

632   that stability parameters which included information about turbulence from SODAR were

633   slightly more accurate. Likewise, [62] found uncertainty with using wind shear to predict the

634   mean wind speed profile, particularly during stable regimes.

635   Turbulence intensity magnitudes were very sensitive to the type of instrument used (cup

636   anemometer versus SODAR), as well as to the methodology chosen to calculate horizontal

637   turbulence when using a SODAR system. We calculated SODAR horizontal turbulence using

638   two methods. The first method used the average of the u and v fluctuations, while the second

639   method used the square-root of the sum of u and v fluctuations squared. The second calculation

640   is used by micrometeorologists, while the first appears to be the primary method used in the

641   wind energy industry. I observations presented here are comparable in magnitude to other wind

642   energy studies [6, 30, 31] when turbulence intensity was measured either with a cup anemometer

643   or the averaging method ($I_{U1SODAR}$). In contrast, a larger range of horizontal turbulence intensity

644   values was observed with the square-root method, and maximum $I_{U2SODAR}$ values exceed I_{Ucup}

645   values published in the literature. This disparity can be attributed to a couple of factors: (1) the

646   fluctuations in horizontal wind speed observed by SODAR were larger than those observed with

647   the cup anemometers at this wind farm, and (2) the averaging-method used in calculating

648    $I_{U1SODAR1}$ (Eq 7) assumes that turbulence is isotropic and that fluctuations in the u and v velocities

649   should be weighted equally, while the square-root method (Eq 8) makes no such assumptions.

650   We believe that $I_{U2SODAR}$ is the best representation of the actual amount of turbulence present in

651   the horizontal direction because it is a calculation of total, not average, horizontal turbulence.

652   Moreover, the amount of diurnal variability in I_U resembled the diurnal variability in *TKE*, when

653    $I_{U2SODAR}$ was chosen to represent horizontal turbulence intensity. Smaller amounts of diurnal

654   variability in I_{Ucup} and $I_{U1SODAR}$ made it difficult to use these parameters to isolate two important

655   stability classes: very stable from stable and very convective from convective.

656   Anemometer differences, including low variance in cup anemometer observations, also

657   have been reported by [63] using controlled flow in wind tunnel experiments. We stress that cup

658   anemometers are not suitable for making turbulence measurements because of their design. Cup

659   anemometers respond faster to increases in velocity than to decreases [48, 64], which can cause a

660   typical cup anemometer to fail to measure 5% of the turbulent energy [60]. On the other hand,

661   [31] also note a difference between SODAR and cup anemometer turbulence intensities and

662   attribute it to the fact that SODAR measurements are noisy. Precipitation is a primary source of

663   noise because sound can be scattered from raindrops back to the SODAR. Precipitation

664   accounted for our lower SODAR data recovery rates during the autumn and winter months. In

665   order to reduce this source of error from the SODAR dataset, we removed moderate-to-high

666   precipitation data points and focused our data analysis on the relatively dry spring and summer

667   seasons.

668   In addition, there are fundamental differences in the way SODAR and cup anemometers

669   measure wind speed, which may have led to the observed differences in I. SODAR measures

670   vectors over a volume average while a cup anemometer does scalar averaging on a point

671   measurement. Vector averaging can be up to 5% lower than scalar averaging, although the mean

672   difference is around 2 to 3% [65]. Assuming equal variance between the two instruments, a

673   lower wind speed would bias the SODAR I magnitudes towards greater values.   SODAR

674   systems also have error due to the fact that beam separation increases with height. These errors

675   are on the order of 0% to 20% [66]. Furthermore, the equations used to calculate horizontal

676   wind speed from SODAR data assume a constant tilt angle between the latitudinal and

677   longitudinal beams and the vertical acoustic beam and a non-zero vertical velocity. There is a

678   chance that non-ideal conditions (e.g., non-flat terrain or the presence of strong buoyant

679   thermals) at this wind farm caused small errors in σ_U, whereby some of the vertical velocity

680   energy was "miss-measured" as part of the horizontal wind speed. To reduce this potential bias

681   in the SODAR data, so that we more accurately describe the turbulence conditions at our site, we

682   also calculated turbulence kinetic energy, which incorporates the velocity fluctuations in all three

683   directions. If there is a bias in the horizontal components of turbulence because of the reasons

684   described above, the error was removed by calculating a measure of total turbulence or *TKE*.

685   $I_{U2SODAR}$ did prove to be an accurate, on-site stability parameter for this wind farm as

686   indicated by the high agreement with *L* and the significant correlations between wind speed and

687   its derived stability regimes. Wind speed increased sharply with height during stable conditions,

688   was nearly uniform or decreased slightly with height during convective conditions, and was near-

689   logarithmic under neutral conditions. Profiles of the three-dimensional turbulent kinetic energy

690   also showed a strong dependency on atmospheric stability. During stable regimes, *TKE*

691   decreased with height indicating that turbulence was mechanically produced at the surface by

692   friction. In contrast, during convective conditions, *TKE* sharply increased with height –

693   convective eddies form near the surface and rise aloft, and only the largest and most energetic

694   eddies rise to higher altitudes. This behavior is consistent with detailed investigations into the

695   planetary boundary layer [67-69]. These stability profiles also agree with other wind power

696   studies [27, 31], which report that wind conditions differ above and below the turbine hub

697   according to stability regime.

698   In very stable conditions, wind shear on the underside of a low level jet may produce

699   intense, coherent, top-down forced turbulence [70]. This turbulence is transported downward by

700   small scale eddies. We found little evidence of turbulence produced aloft, such as a significant

701   peak in *TKE* at the top of the rotor, although we did observe increasing wind speeds aloft (100 to

702   120 m), which indicated the possible presence of nocturnal low-level jets. The lack of strong

703   *TKE* maxima at the top of the nighttime profiles during very stable conditions may be due to

704 several reasons. First, the downward transport of turbulence is, by nature, very intermittent [14]

705 and the instrument sampling frequency may have acted as a low pass filter and missed these

706 events. Second, LLJs could have occurred at heights above the maximum SODAR measurement

707 height ($z > 200$ m). And finally, our seasonal averaging would eliminate evidence of low-level

708 jets if LLJs did not occur regularly each night.

709 It is our observation that wind speed and turbulence kinetic energy predictably vary with

710 height depending on atmospheric stability. Therefore, there are numerous advantages to

711 deploying sophisticated meteorological instruments at large wind farms, instead of relying on

712 cup anemometers for sparse measurements of wind speed and turbulence intensity at hub-height

713 and possibly at one or more heights in the rotor disk. The high-resolution SODAR data

714 confirmed that a constant wind shear exponent, as assumed by the power law, leads to grossly

715 inaccurate predictions of wind speeds at the top and bottom of the rotor disk, particularly during

716 strongly stable or strongly convective conditions. These inaccuracies can be either over-

717 assessments of the wind resource (as seen in the turbulent time periods at this site) or under-

718 assessments of the wind resource (as seen in the stable time periods at this site) and are

719 consistent with findings in [45]. Considering that the accuracy of wind speed across the entire

720 rotor disk is critical to wind energy applications, we recommend that wind farms invest in more

721 sophisticated meteorological instrumentation, such as remote sensing platforms, which give high

722 spatial resolution velocity and turbulence measurements. Furthermore, our results strongly

723 suggest that on-site, near-real-time estimates of stability would enable a wind farm to more

724 accurately predict the available wind resource.

725

Conclusions

The main scientific conclusions that can be drawn from this study are:

(1) Local atmospheric stability in the lower planetary boundary layer can be quantified at wind farms in mildly complex terrain. Stability can be assessed by measuring wind shear across heights equal to the rotor disk or by measuring turbulence at heights equivalent to the rotor disk. Accurate measurements of turbulence require either a remote-sensing platform or sonic anemometer. Either hub-height equivalent turbulence intensity (using the square-root method) or turbulence kinetic energy can be used as a turbulence stability parameter. Although, *TKE* is theoretically superior to *I* because it is an absolute (not relative) measure of turbulence and includes all 3-dimensional fluctuations in wind speed. We emphasize that all 3-dimensional fluctuations in wind speed have the potential to impact wind turbine performance.

(2) Vertical profiles of mean wind speed and turbulence across heights equivalent to the rotor disk are strongly correlated to atmospheric stability as seen in the high-resolution SODAR observations. Basing the available wind resource on hub-height wind speed without correcting for stability leads to either over-assessments of the wind resource during convective periods or under-assessments of the wind resource during stable regimes at this onshore wind farm.

761

762

763

764

765

766

767

768

769

770 **References**

771

772 1. DOE Wind and Water Power Program, *Wind Power Today 2010*. Downloaded from
773 http://www1.eere.energy.gov/windandhydro/pdfs/47531.pdf on 25 May 2010.

774 2. Enercon, World's most powerful wind turbine installed near Emden, *Windblatt Magazine*
775 2007; **4**: 6-7. Downloaded from
776 http://www.enercon.de/www/en/windblatt.nsf/vwAnzeige/66BD14BABA22BCA2C1257
777 3A7003FA82E/$FILE/WB-0407 on 27 October 2010.

778 3. Larsen SE, Gryning SE, Jensen NO, Jorgensen HE, Mann J. Mean wind and turbulence
779 in the atmospheric boundary layer above the surface layer. *In*: *Wind Energy*, *Proceedings*
780 *of the Euromech Colloquium* (Eds.) Peinke J, Schaumann P, Barth S. Springer Berlin
781 Heidelberg: New York, 2007; 21-25.

782 4. Elliott DL, Cadogan JB. Effects of wind shear and turbulence on wind turbine power
783 curves. *In*: Scientific proceedings. European Community Wind Energy Conference and
784 Exhibition, Madrid (Spain), 1990.

785 5. Motta M, Barthelmie RJ, Vølund P. The influence of non-logarithmic wind speed
786 profiles on potential power output at Danish offshore sites. *Wind Energy* 2005; **8**: 219-
787 236.

788 6. Sumner J, Masson C. Influence of atmospheric stability on wind turbine power
789 performance curves. *J. Sol. Energy Eng.* 2006; **128**: 531-537.

790 7. Gottschall J, Peinke J. How to improve the estimation of power curves for wind turbines.
791 *Environ. Res. Lett.* 2008; **3**: 1-7.

792 8. van den Berg GP. Wind turbine power and sound in relation to atmospheric stability.
793 *Wind Energy* 2008; **11**: 151-169.

794 9. Antoniou I, Pedersen SM, Enevoldsen PB. Wind shear and uncertainties in power curve
795 measurement and wind resources. *Wind Eng.* 2009; **33**: 449-468.

796 10. Tennekes H. Similarity relations, scaling laws and spectral dynamics. *In*: *Atmospheric*
797 *Turbulence and Air Pollution Modeling*. (Eds.) Nieuwstadt FTM, van Dop H. Reidel:
798 Dordrecht, 1982; 37-68.

799 11. Blumen W, Banta R, Burns SP, Fritts DC, Newsom R, Poulos GS, JL Sun. Turbulence
800 statistics of a Kelvin-Helmholtz billow event observed in the night-time boundary layer
801 during the Cooperative Atmosphere-Surface Exchange Study Field. *Dyn. Atmos. Oceans*
802 2001; **34**: 189-204.

803   12.   Panofsky HA, Dutton JA. *Atmospheric Turbulence – Models and Methods for*
804   *Engineering Applications*. John Wiley & Sons: New York, 1984; 397 pp.

805   13.   Kaimal JC, Finnigan JJ. *Atmospheric Boundary Layer Flows – Their Structure and*
806   *Measurement*. Oxford University Press: New York, 1994; 287 pp.

807   14.   Mahrt L, Sun J, Blumen W, Delany T, Oncley S. Nocturnal boundary-layer regimes.
808   *Boundary-layer Meteorol.* 1998; **88**: 255-278.

809   15.   Mahrt L. Stratified atmospheric boundary layers. *Boundary-layer Meteorol.*1999; **90**:
810   375-396.

811   16.   Mahrt L, Vickers D. Contrasting vertical structures of nocturnal boundary layers.
812   *Boundary-layer Meteorol*. 2002; **105**: 351-363.

813   17.   Stull RB. *An Introduction to Boundary Layer Meteorology*. Kluwer Academic Publishers:
814   Dordrecht, The Netherlands, 1988, 670 pp.

815   18.   Joffre SM. Power laws and the empirical representation of velocity and directional shear.
816   *J Climate and Applied Meteor.* 1984; **12**: 1196-1203.

817   19.   Heald RC, Mahrt L. The dependence of boundary-layer shear on diurnal variation of
818   stability. *J Applied Meteor.* 1981; **20**: 859-867.

819   20.   Kelley ND, Osgood RM, Bialasiewisz JT, Jakubowski A. Using wavelet analysis to
820   assess turbulence/rotor interactions. *Wind Energy* 2001; **3**: 121-134.

821   21.   Hand MM, Kelley ND, Balas MJ. *Identification of Wind Turbine Response to Turbulent*
822   *Inflow Structures*. NREL/CP-500-33465, 2003.

823   22.   Blackadar AK. Boundary layer wind maxima and their significance for the growth of
824   nocturnal inversions. *Bull. Am. Meteorol. Soc.* 1957; **38**: 283-290.

825   23.   Banta RM. Stable-boundary-layer regimes from the perspective of the low-level jet. *Act.*
826   *Geophys.* 2008; **56**: 58-87.

827   24.   Kelley ND, Shirazi M, Jager D, Wilde S, Adams J, Buhl M, Sullivan P, Patton E. *Lamar*
828   *Low-Level Jet Project Interim Report*. NREL/TP-500-34593. Golden, CO, National
829   Renewable Laboratory, 2004; 216 pp.

830   25.   Emeis S, Harris M, Banta RM. Boundary-layer anemometry by optical remote sensing
831   for wind energy applications. *Meteor. Zeitschr.* 2007; **16**: 337-347.

832   26.   Cosack N, Emeis S, Kuhn M. On the influence of low-level jets on energy production and
833   loading of wind turbines. *In*: *Wind Energy, Proceeding of the Euromech Colloquium*

834   (Eds.) Peinke J, Schaumann P, Barth S. Springer Berlin Heidelberg: New York, 2007;
835   325-328.

836 27. Pichugina YL, Banta RM, Kelley ND, Brewer WA, Sandberg SP, Machol JL, Jonkman
837   BJ. Remote sensing of the nocturnal boundary layer for wind energy applications.
838   14th Internat. Sympos. for the Advancement of Boundary Layer Remote Sensing, IOP
839   Conf. Series: *Earth and Environmental Science* 2008; **1**: doi:10.1088/1755-
840   1307/1/1/012048.

841 28. Storm B, Dudhia J, Basu S, Swift A, Giammanco I. Evaluation of the weather research
842   and forecasting model on forecasting low-level jets: implications for wind energy. *Wind*
843   *Energy* 2009; **12**: 81-90.

844 29. Hunter R, Pedersen TF, Dunbabin P, Antoniou A, Frandsen S, Klug H, Albers A, Lee
845   WK. *European wind turbines testing procedure developments. Task 1: Measurement*
846   *Method to Verify Wind Turbine Performance Characteristics.* Risø National Laboratory,
847   Roskilde, RISØ R-1209(EN), 2001; 120 pp.

848 30. Rareshide E, Tindal A, Johnson C, Graves AM, Simpson E, Bleeg J, Harris T, Schoborg
849   D. Effects of complex wind regimes on turbine performance. *In*: Scientific proceedings.
850   American Wind Energy Association WINDPOWER Conference, Chicago, Ill (USA),
851   2009.

852 31. Wagner R, Antoniou I, Pedersen SM, Courtney MS, Jørgensen HE. The influence of the
853   wind speed profile on wind turbine performance measurements. *Wind Energy* 2009; **12**:
854   348-362.

855 32. Kaiser K, Hohlen H, Langreder W. Turbulence correction for power curves. *In*: Scientific
856   proceedings. European Wind Energy Conference and Exhibition, Madrid (Spain),
857   2003.

858 33. Honhoff S. Power Curves − The effect of environmental conditions. *In*: Scientific
859   proceedings. GE Wind, AWEA Wind Speed and Energy Workshop, Portland, OR
860   (USA), 2007.

861 34. Tindal A, Johnson C, LeBlanc M, Harman K, Rareshide E, Graves A-M. Site-specific
862   adjustments to wind turbine power curves. *In*: Scientific proceedings. American Wind
863   Energy Association WINDPOWER Conference, Houston, Texas (USA), 2008.

864 35. International Electromechanical Commission (IEC). *Wind Turbines - Part 12-1: Power*
865   *performance measurements of electricity producing wind turbines.* Technical Report No,
866   IEC 61400-12-1, 2005.

867   36.   Coulter RL, Kallistratova MA. The role of acoustic sounding in a high-technology era.
868   *Meteor. Atmos. Phys.* 1999; **71**: 3-13.

869   37.   Crescenti GH. A look back on two decades of Doppler sodar comparison studies. *Bull.*
870   *Am. Meteorol. Soc.* 1997; **78**: 651-673.

871   38.   Antoniou I, Jørgensen HE, Ormel F, Bradley S, von Hünerbein S, Emeis S, Warmbier G.
872   On the Theory of SODAR Measurement Techniques. Risø National Laboratory:
873   Roskilde, Denmark, 2003, 59 pp.

874   39.   Sutton OG. *Atmospheric Turbulence*. Methuen & Co. Ltd.: London, 1949; 107 pp.

875   40.   Elliott DL, Holliday C, Barchet W, Foote H, Sandusky W. *Wind Energy Resource Atlas*
876   *of the United States*. DOE/CH 10093-4, Golden, Colorado: Solar Energy Research
877   Institute, 1987, 210 pp.

878   41.   Rohatgi J. An analysis of the influence of atmospheric stability on vertical wind profiles
879   – its influence on wind energy and wind turbines. *Wind Eng.* 1996; **20**: 319-332.

880   42.   Scrase FJ Some characteristics of eddy motion in the atmosphere. Meteorological Office,
881   *Geophysical Memoir* 1930; **52**.

882   43.   Justus CG, Mikhail A. Height variation of wind speed and wind distributions statistics.
883   *Geophys. Res. Lett.* 1976; **3**: 261-264.

884   44.   Peterson EW, Hennessey JP. On the use of power laws for estimates of wind power
885   potential. *J. Appl. Meteorol.* 1977; **17**: 390-394.

886   45.   Sisterson DL, Hick BB, Coulter RL, Wesely ML. Difficulties in using power laws for
887   wind energy assessment. *Solar Energy* 1983; **31**: 201-204.

888   46.   Shaw RH, Hartog GD, King KM, Thurtell GW. Measurements of mean wind flow and
889   three-dimensional turbulence intensity within a mature corn canopy. *Agric. Meteorol.*
890   1974; **13**: 419-425.

891   47.   Chan PW. Measurement of turbulence intensity profile by a mini-sodar. *Meteorol. Appl.*
892   2008; **15**: 249-258.

893   48.   Weber RO. Estimators for the standard deviations of lateral, longitudinal, and vertical
894   wind components. *Atmos. Environ.* 1998; **32**: 3639-3646.

895   49.   Piper M, Lundquist JK. Surface layer turbulence measurements during a frontal passage.
896   *J. Atmos. Sci.* 2004; **61**: 1768-1780.

897   50.   Mahrt L, Vickers D, Nakamura R, Soler MR, Sun J, Burns S, Lenschow DH. Shallow
898   drainage flows. *Boundary-layer Meteorol.* 2001; **101**: 243-260.

899 51. Lundquist JK. Intermittent and elliptical inertial oscillations in the atmospheric boundary
900 layer. *J. Atmos. Sci.* 2003; **60**: 2661-2673.

901 52. Lundquist JK, Mirocha JD. Interaction of nocturnal low-level jets with urban geometries
902 as seen in Joint Urban 2003 data. *J. Appl. Meteorol. Clim.* 2008; **47**: 44-58.

903 53. Monin AS, Obukhov AM. Basic laws of turbulent mixing in the ground layer of the
904 atmosphere. *Trans. Geophys. Inst.* 1954; **151**: 163-187.

905 54. Obukhov AM. Turbulence in an atmosphere with a non-uniform temperature. *Boundary-*
906 *layer Meteor.* 1971; **2**: 7-29.

907 55. Nieuwstadt FTM. The turbulent structure of the stable, nocturnal boundary layer. *J*
908 *Atmos. Sci.* 1984; **41**: 2202-2216.

909 56. van Wijk AJM, Beljaars ACM, Holtslag AAM, and Turkenburg WC. Evaluation of
910 stability corrections in wind speed profiles over the North Sea. *J. Wind Eng. Ind.*
911 *Aerodyn.* 1990; **33**: 551-566.
912
913 57. Sathe A, Bierbooms W. Influence of different wind profiles due to varying atmospheric
914 stability on the fatigue life of wind turbines. *J. Phys. Conference Series* 2007; **75**: 1-7.

915 58. Walter K, Weiss CC, Swift A, Chapman J, Kelley ND. Speed and direction shear in the
916 stable nocturnal boundary layer. *J. Sol. Energy Eng.* 2009; **131**: 1-7.

917 59. Langreder W, Højstrup J, Kaiser K, Hohlen H. Turbulence correction for power curves.
918 *In*: Scientific proceedings. European Wind Energy Conference and Exhibition,
919 London (GB), 2004.

920 60. Pedersen BM, Pedersen TF, Klug H, van der Borg N, Kelley N, Dahlberg JA. Wind
921 *Speed Measurement and Use of Cup Anemometry. In:* Recommended Practices for Wind
922 Turbine Testing and Evaluation. (Ed) RS Hunter, 1999, 49 pp.

923 61. Lu X, McElroy MB, Kiviluoma J. Global potential for wind-generated electricity. *Proc.*
924 *Nat. Acad. Sci.* 2009; **106**: 10933-10938.

925 62. Sisterson DL, Frenzen P. Nocturnal boundary-layer wind maxima and the problem of
926 wind power assessment. *Environ. Sci. Technol.* 1978; **12**: 218-221.

927 63. Yahaya S, Frangi JP. *Spectral Response of Cup Anemometers*. Laboratoire
928 Environmmement et Developpement Report, Universite Paris, 2003; 1-3.

929 64. Hölling M, Schulte B, Barth S, Peinke J. Sphere anemometer – a faster alternative
930 solution to cup anemometry. The Science of Making Torque from Wind. *J. Phys.*
931 *Conference Series* 2007; **75**: 012064.

932   65.   Moore KE, Bailey BH. *Recommended practices for the use of SODAR in wind energy*
933   *resource assessment.* Integrated Environmental Data, LLC, 2009; 1-13.

934   66.   von Hünerbein S, Antoniou I, Bradley SG, Jørgensen HE, Kindler D. Calibration of
935   SODARs for wind energy applications. International Symposium for the Advancement
936   of Boundary Layer Remote Sensing, Garmisch-Partenkirchen (Germany), 2006.

937   67.   Hicks BB. Wind profile relationships from Wangara Experiment. *Quart. J. Roy. Meteor.*
938   *Soc.* 1976; **102**: 535-551.

939   68.   André J-C, De Moor G, Lacarrère P, Therry G, du Vachat R. Modeling the 24-hour
940   evolution of the mean and turbulent structure of the planetary boundary layer. *J. Atmos.*
941   *Sci.* 1978; **35**: 1861-1883.

942   69.   Poulos GS, Blumen W, Fritts DC, Lundquist JK, Sun J, Burns SP, Nappo C, Banta R,
943   Newsom R, Cuxart J, Terradellas E, Balsley B, Jensen M. CASES-99: A comprehensive
944   investigation of the stable nocturnal boundary layer. *Bull. Am. Meteorol. Soc.* 2002;
945   **83**:555-581.

946   70.   Smedman A-S. Observations of a multi-level turbulence structure in a very stable
947   atmospheric boundary layer. *Boundary-layer Meteor.* 1988; **44**: 231-253.

948

949

950

951

952

953

954

955

956

957

958

959

960

961   **Table headings**

962

963   **Table 1.** List of available meteorological instrumentation, variables measured, and measurement

964   heights.

965

966   **Table 2.** Stability criteria for the direct stability parameter Obukhov length and five on-site

967   stability parameters: wind shear exponent, cup anemometer turbulence intensity, SODAR

968   turbulence intensity ("averaging method"), SODAR turbulence intensity ("square-root method"),

969   and turbulence kinetic energy, as well as general atmospheric conditions for each stability

970   regime. Note that neutral conditions also include weakly stable and weakly convective. *I* and

971   *TKE* are at 80 m; α is from 40m to 120 m.

972

973

974

975

976

977

978

979

980

981

982

983

984

985 **Figure headings**

986

987 **Figure 1.** Illustration of the wind park and relative locations of meteorological instrumentation

988 and turbines used in this analysis. The SODAR was a roving system and SODAR1, SODAR2,

989 and SODAR3 correspond to different time periods.

990

991 **Figure 2.** Seasonal mean (± one standard deviation) normalized power (a) and nacelle (80 m)

992 wind speed (b) for a single turbine at the wind farm. Hub-height wind speeds during the spring

993 and summer were on average 3 m s^{-1} higher than during the cooler months, while normalized

994 power values were on average 30-35% greater.

995

996 **Figure 3.** Mean diurnal normalized power at a single turbine by season shows large power

997 differences at night, between spring/summer periods and winter/autumn periods, which approach

998 50%. Smaller power differences are also observed during the daytime hours.

999

1000 **Figure 4.** Mean nighttime and daytime wind speeds at 40 m, 80 m, and 120 m show a strong

1001 seasonality towards peak wind speeds in the summer and strong shear at night. Also noticeable

1002 are wind speed differences between the SODAR (a) and meteorological tower cup anemometers

1003 (b), particularly during the daytime. The meteorological tower is not instrumented at 120 m.

1004

1005 **Figure 5.** Frequency plots of nighttime/daytime wind direction for 40 m, 80 m, and 120 m wind

1006 speed during February (a-c) and July (d-f). Nighttime wind direction is predominately from the

1007 west-southwest in both months. During the winter, a secondary peak in daytime winds is

1008 observed from the northeasterly direction while during the summer WSW winds dominate. Very

1009 little directional wind shear with height is evident regardless of month or time of day.

1010

1011 **Figure 6.** Percentage of spring and summer 10-minute periods classified as stable, neutral or

1012 convective according to the stability parameters: (a) Obukhov length, (b) SODAR wind shear

1013 exponent, (c) cup anemometer I_U, (d) SODAR I_{U1}, (e) SODAR I_{U2}, and (f) SODAR turbulence

1014 kinetic energy. *I* and *TKE* were measured at heights equivalent to hub-height, while α represents

1015 heights across the entire rotor-disk. The stability parameters with highest agreement to *L* are *TKE*

1016 and SODAR I_{U2}.

1017

1018 **Figure 7.** Box-plot histogram of 10-minute (a) wind shear exponent *(α_{40_120})*, (b) hub-height

1019 turbulence intensity ($I_{U2SODAR}$), and (c) hub-height turbulence kinetic energy (*TKE*) data

1020 according to *z/L* stability class show good agreement between the three, on-site SODAR stability

1021 parameters and the normalized Obukhov length. The box-plot histogram shows the mean (small

1022 square), median (horizontal line), 25th and 75th percentiles (bottom and top of the box), 5th and

1023 95th percentiles (lower and upper whisker line), and 1st and 99th percentiles (x symbols).

1024

1025 **Figure 8.** Mean diurnal plot of (a) the normalized Obukhov length, (b) wind shear exponent, (c)

1026 cup anemometer turbulence intensity, (d) SODAR turbulence intensity $I_{U1SODAR}$, (e) SODAR

1027 turbulence intensity $I_{U2SODAR}$, and (f) turbulence kinetic energy during the spring and summer

1028 months. All parameters show convective conditions during the day and stable conditions at night

1029 in agreement with z/L while α_{120_40}, $I_{U2SODAR}$, and TKE show the highest amount of diurnal

1030 variability. The gray shading represents stable conditions, x-notched shading is neutral

1031 conditions, and white shading is convective conditions according to the thresholds for each

1032 stability parameter as listed in Table 2.

1033

1034 **Figure 9.** Mean wind speed at heights representative of the turbine rotor disk (40, 80, and 120 m)

1035 according to stability class in (a) spring and (b) summer. The largest stability influences occur

1036 during the summer season when strongly stable and strongly convective wind speeds differ by

1037 more than 10 m s^{-1}. The horizontal lines show the seasonal mean wind speed at each height.

1038

1039 **Figure 10.** Spring vertical profiles (30 m to 150 m) of SODAR (a) mean wind speed and (b)

1040 turbulence kinetic energy during strongly stable, stable, near-neutral, convective, and strongly

1041 convective conditions. For reference, the turbine rotor disk covers heights of 40 to 120 m. The

1042 error bars are ± one standard deviation from the mean. Also plotted in 10a is the predicted wind

1043 speed profile (open circles) based on the 1/7th power law ($\alpha = 0.14$) and the 80 m wind speed.

1044

1045 **Figure 11.** Summer vertical profiles (30 m to 150 m) of SODAR (a) mean wind speed and (b)

1046 turbulence kinetic energy during strongly stable, stable, near-neutral, convective, and strongly

1047 convective conditions. Also plotted in 11a is the predicted wind speed profile (open circles)

1048 based on the 1/7th power law ($\alpha = 0.14$) and 80 m wind speed. Missing data are due to poor data

1049 recovery at those heights.

	Instrument	Averaging time	Location	Measurement height (m)	Measurement	# of site locations
wind speed	cup anemometer	10 min	on-site, turbine nacelle hub	80	U (m/s)	6
	cup anemometer	10 min	on-site, 50 m tall tower	30, 40, 50	U (m/s) σ_U (m/s)	1 array
	cup anemometer	10 min	on-site, 80 m tall tower	50, 60, 80	U (m/s) σ_U (m/s)	1 array
	SODAR	10 min	on-site, remote sensing platform	20-200, every 10 m	u, v, w (m/s) $\sigma_u, \sigma_v, \sigma_w$ (m/s)	3 (one roving system)
	3-D sonic anemometer	30 min	off-site, flux tower	3	$u(t), v(t), w(t)$ (m/s) u, v, w (m/s) u', v', w' (m/s)	1
wind direction	wind vane	10 min	on-site, 50 m tall tower	47	direction (°)	1 (partially inactive)
	wind vane	10 min	on-site, 80 m tall tower	77	direction (°)	1(partially inactive)
	SODAR	10 min	on-site, remote sensing platform	20-200, every 10 m	direction (°)	3 (one roving system)
	3-D sonic anemometer	30 min	off-site, flux tower	3	direction (°)	1
air temperature	temperature sensor	10 min	on-site, 50 m tall tower	47	T_a (°C)	1 (partially inactive)
	temperature sensor	10 min	on-site, 80 m tall tower	77	T_a (°C)	1 (partially inactive)
	Fast-response thermocouple, relative humidity sensor	30 min	off-site, flux tower	3	θ_v (K) RH (%)	1

1052   **Table 1**

1053

1054

1055

1056

1057

1058

1059

1060

Stability class	L (m)	α	I_{Ucup} & $I_{UISODAR}$ (%)	$I_{U2SODAR}$ (%)	TKE (m^2 s^{-2})	Boundary layer properties
strongly stable	0 < L < 100	$\alpha > 0.3$	$I_U < 7\%$	$I_U < 8\%$	$TKE < 0.4$	Highest shear in swept-area, nocturnal LLJ may be present, little turbulence except just below a LLJ
stable	100 < L < 600	$0.2 < \alpha < 0.3$	$7 < I_U < 9\%$	$8 < I_U < 10\%$	$0.4 < TKE < 0.7$	High wind shear in swept-area, nocturnal LLJ may be present, little turbulence except just below a LLJ
neutral	|L| > 600	$0.1 < \alpha < 0.2$	$9 < I_U < 12\%$	$10 < I_U < 13\%$	$0.7 < TKE < 1.0$	Generally strongest wind speeds throughout the blade swept-area, logarithmic wind profile
convective	- 600 < L < - 50	$0.0 < \alpha < 0.1$	$12 < I_U < 14\%$	$13 < I_U < 20\%$	$1.0 < TKE < 1.4$	Lower wind speeds, low shear in swept-area, high amount of turbulence
strongly convective	-50 < L < 0	$\alpha < 0.0$	$I_U > 14\%$	$I_U > 20\%$	$TKE > 1.4$	Lowest wind speeds, very little wind shear in swept-area, highly turbulent

1061   **Table 2**

1062
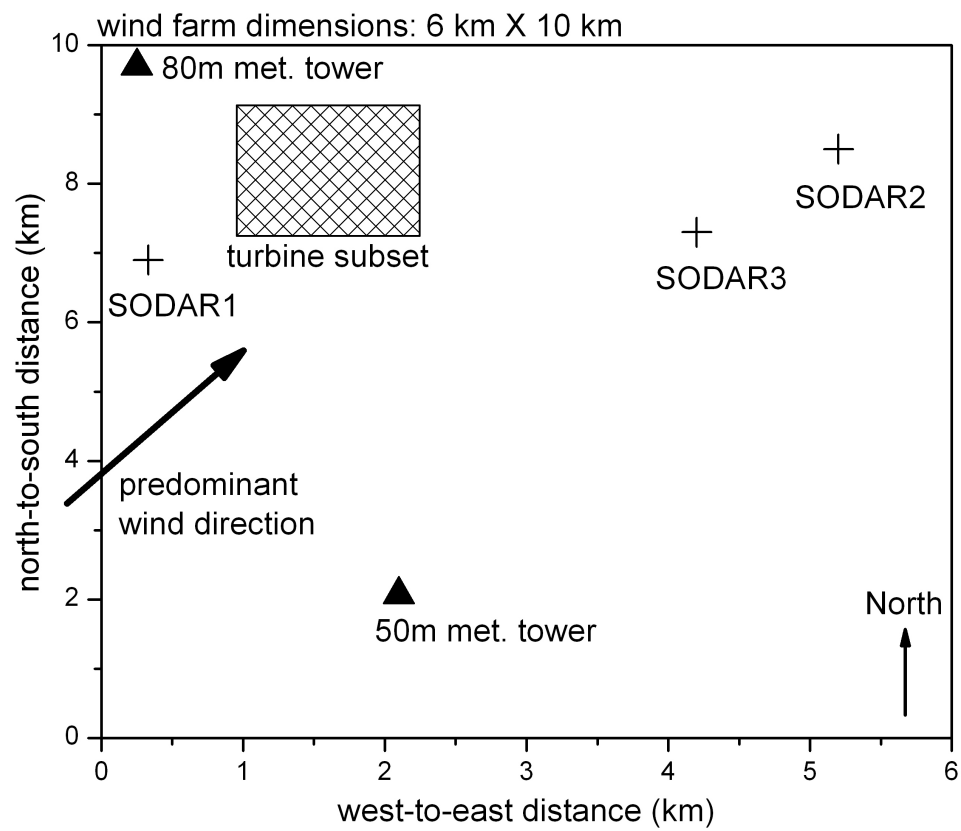
1063

1064

1065

1066

1067

1068

1069

1070

1071

1072

1073

1074

1075

1076

1077

wind farm dimensions: 6 km X 10 km

1078

1079 **Figure 1**

1080

1081

1082

1083

1084

1085

1086
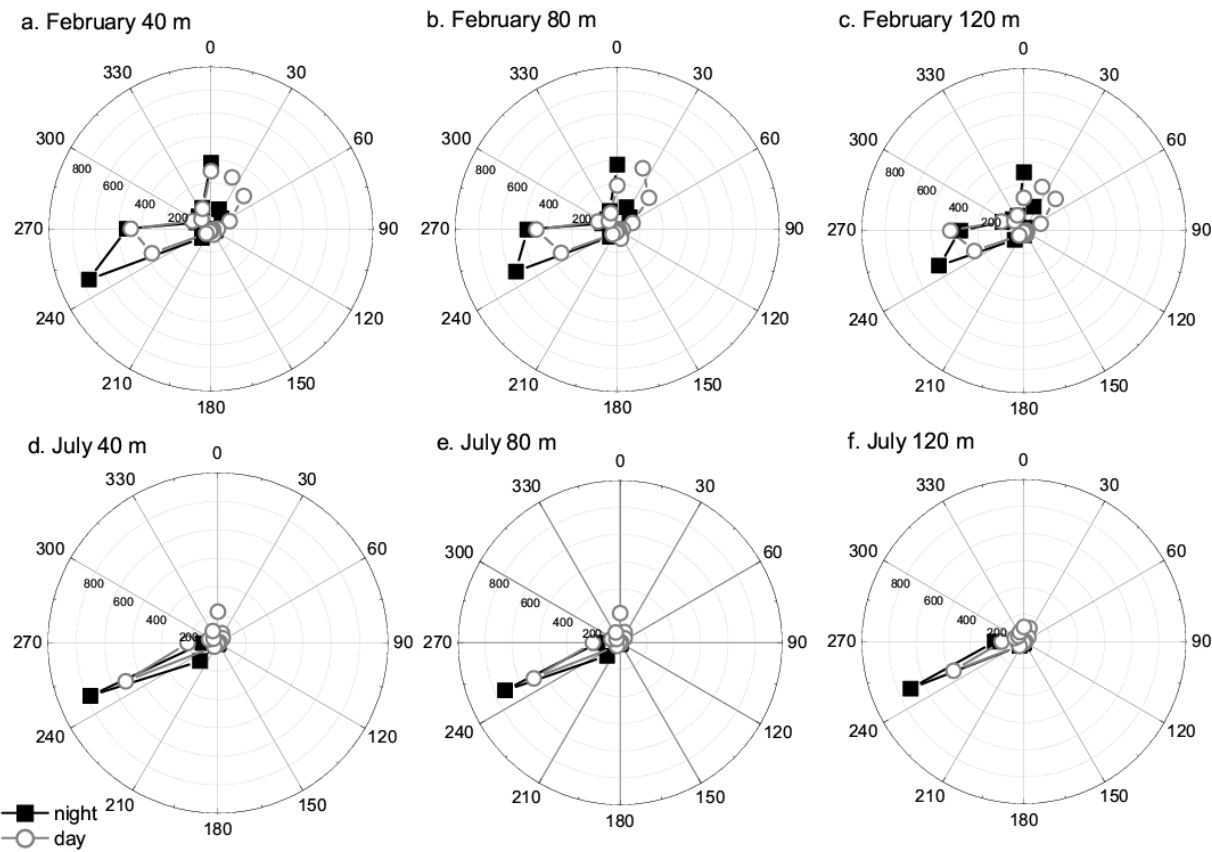
1087

1088

1089

1090

1091 **Figure 2**

1092

1093

1094

1095

1096   **Figure 3**

1097

1098

1099

1100

1101

1102

1103

1104

1105

1106

1107

Figure 4

1108

1109

1110

1111

1112

1113

1114

1115

1116

1117

1118

1119

1120

1121

1122

1123

a. February 40 m   b. February 80 m   c. February 120 m

d. July 40 m   e. July 80 m   f. July 120 m

- ■ — night
- ○ — day
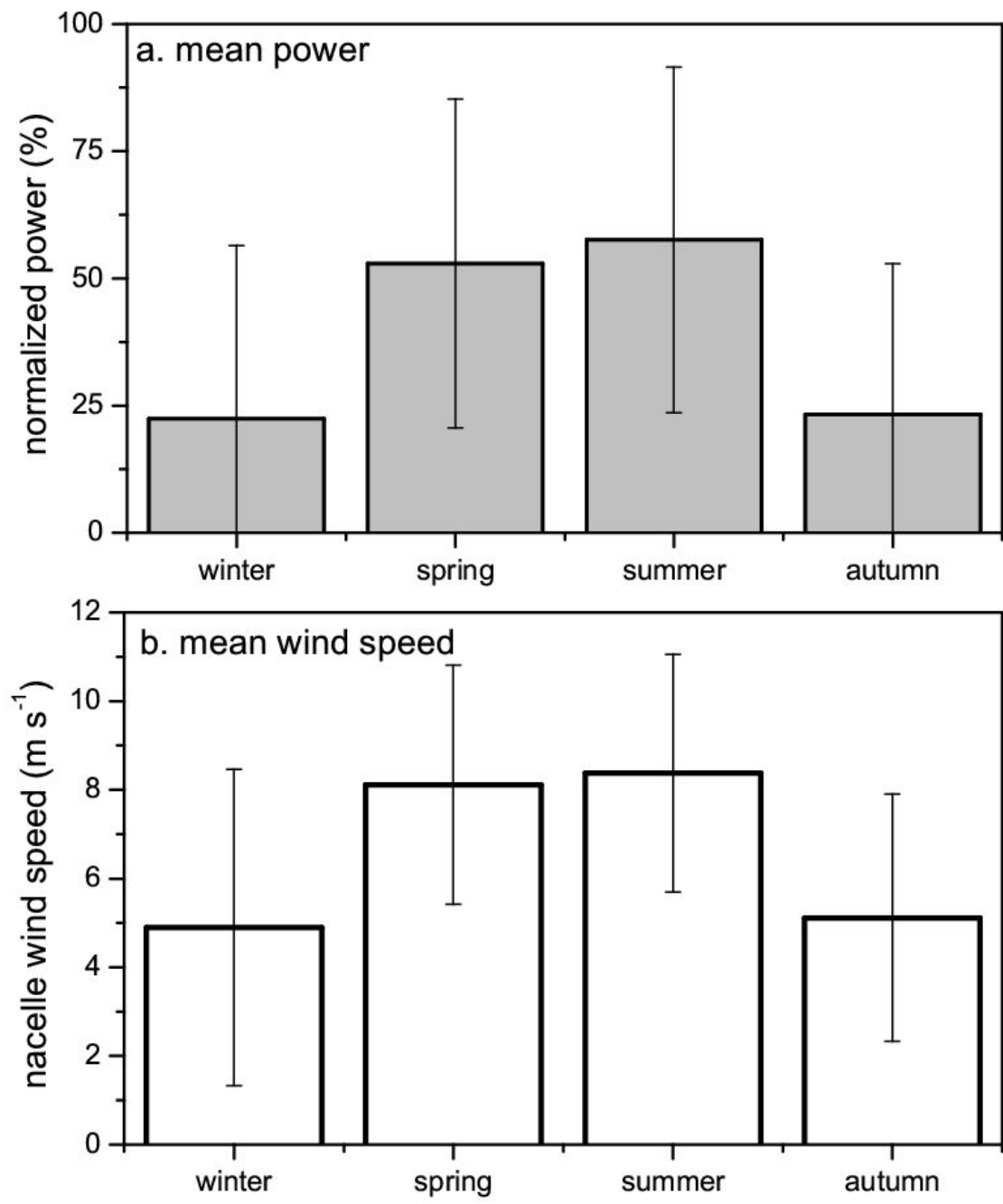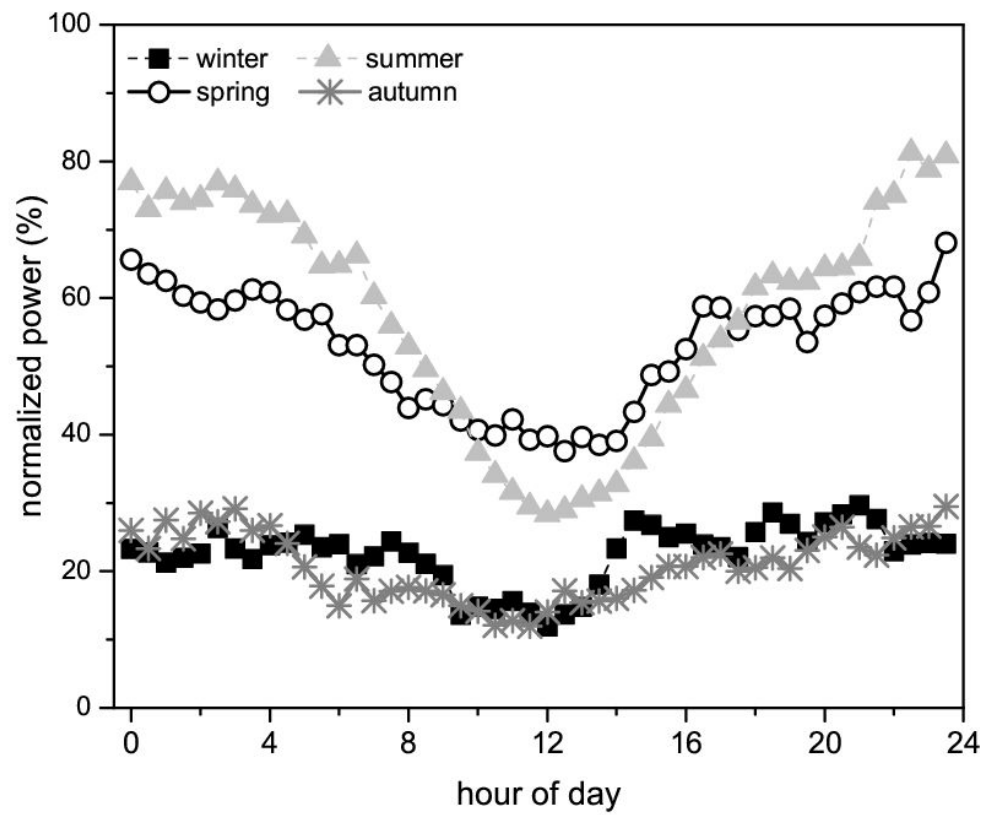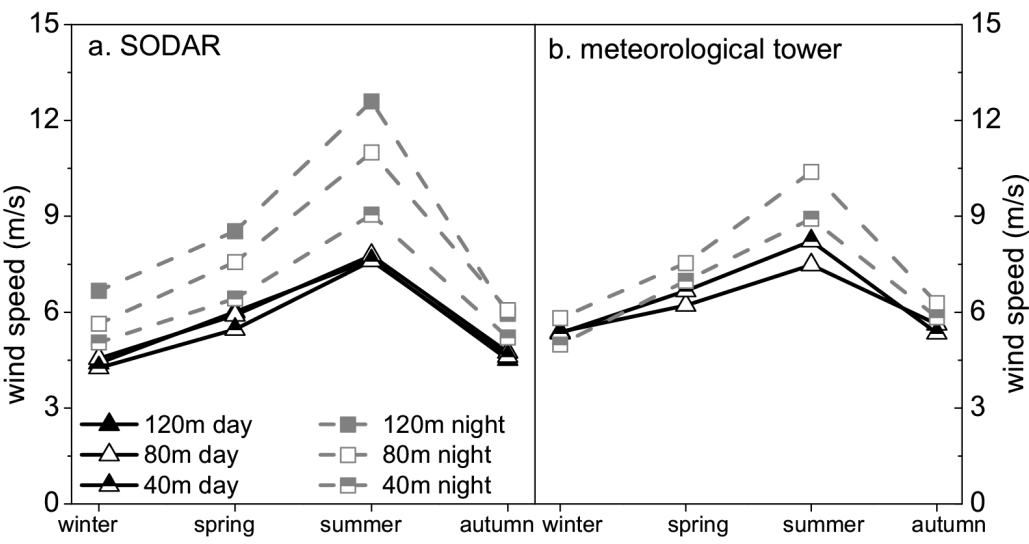
1124

1125 **Figure 5**

1126

1127

1128

1129

1130

1131

1132

1133

1134

1135

1136
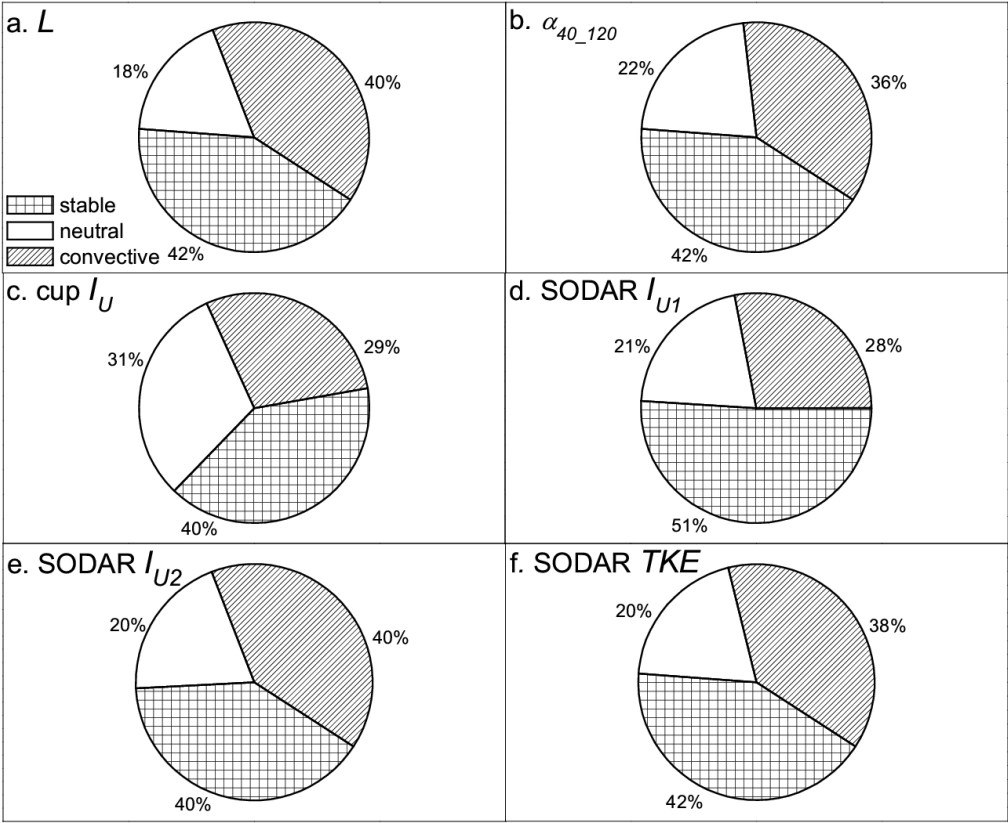
1137

1138 **Figure 6**
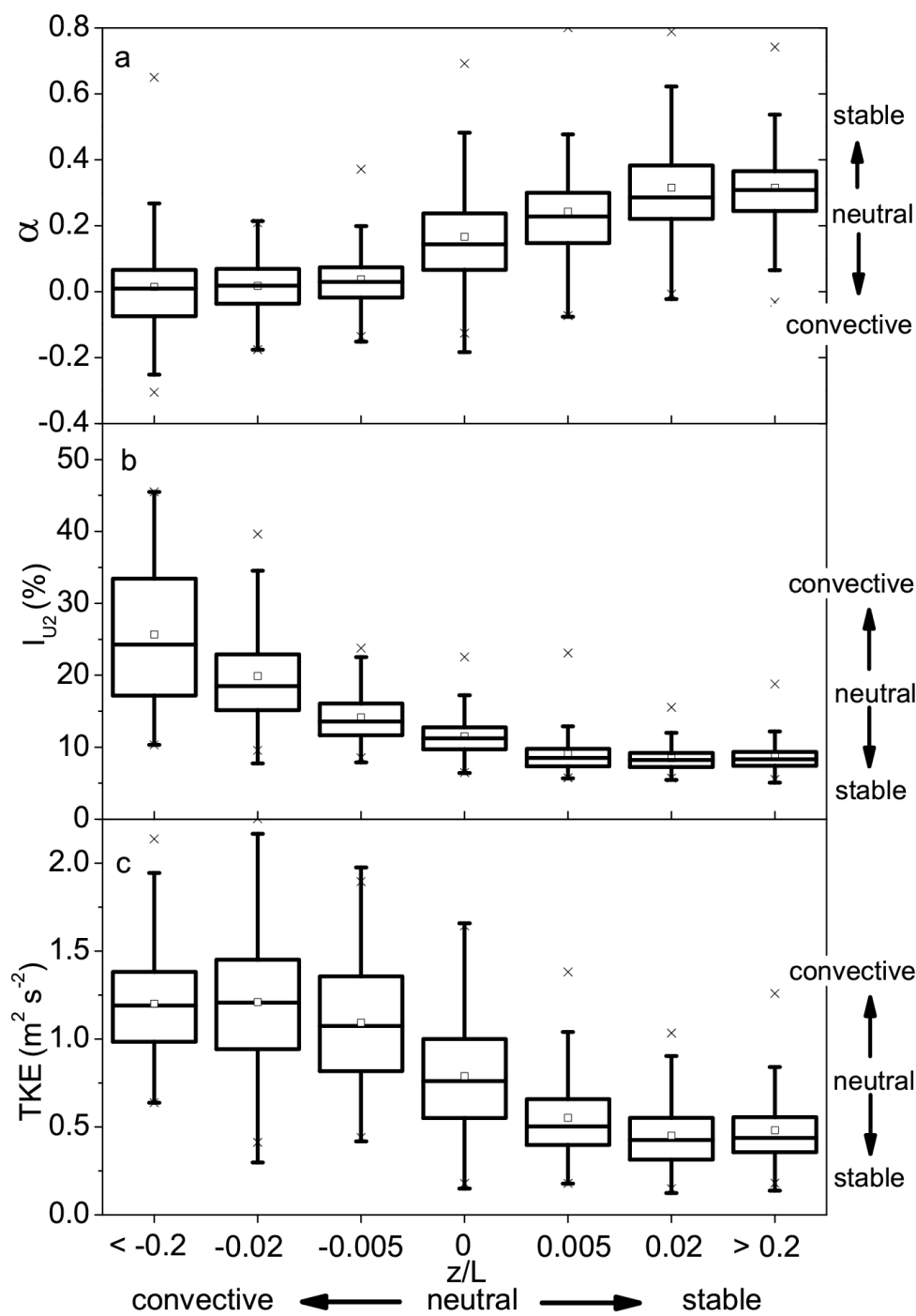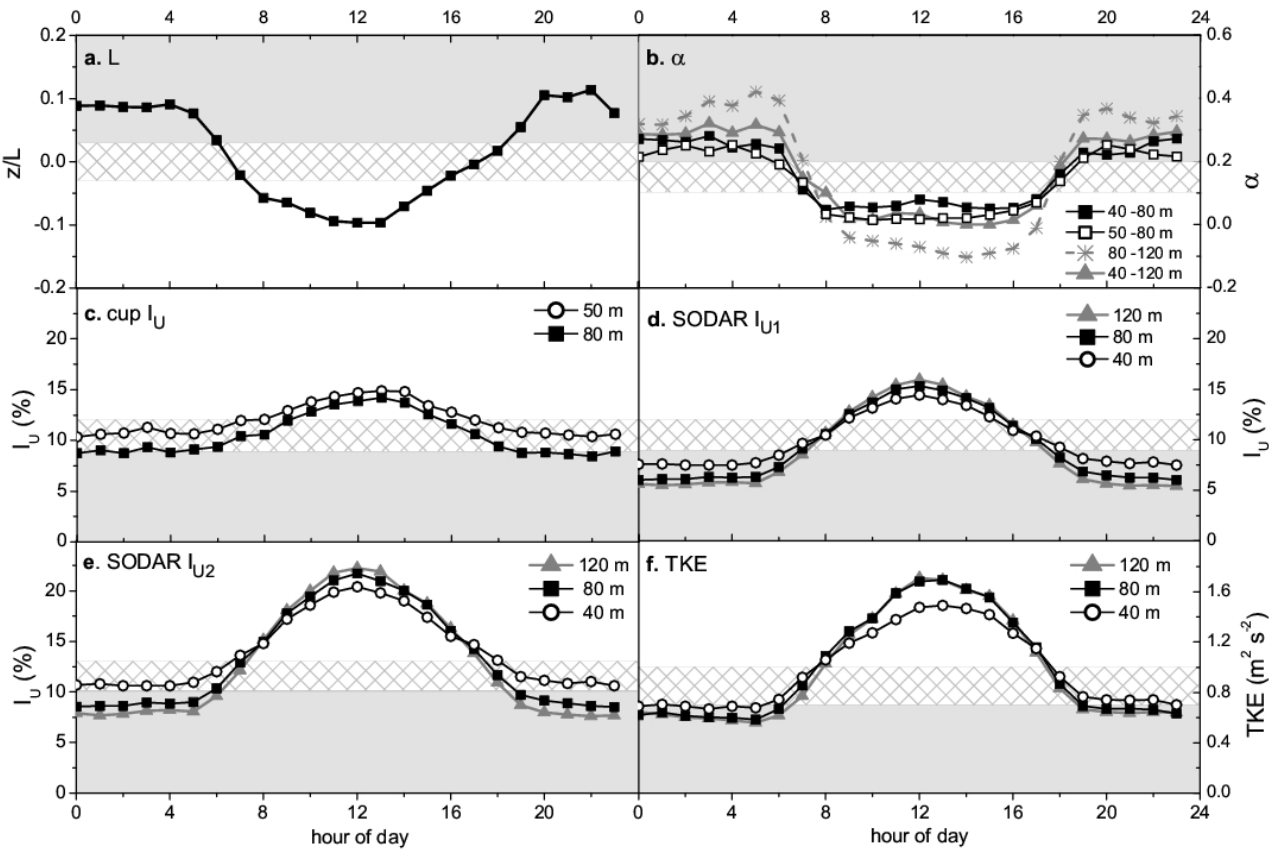
1139

1140

1141

1142

1143

1144

1145

1146

1147

1148

1149

Figure 7

1151

1152

1153

1154

Figure 8

1155

1156

1157

1158

1159

1160

1161

1162

1163

1164

1165
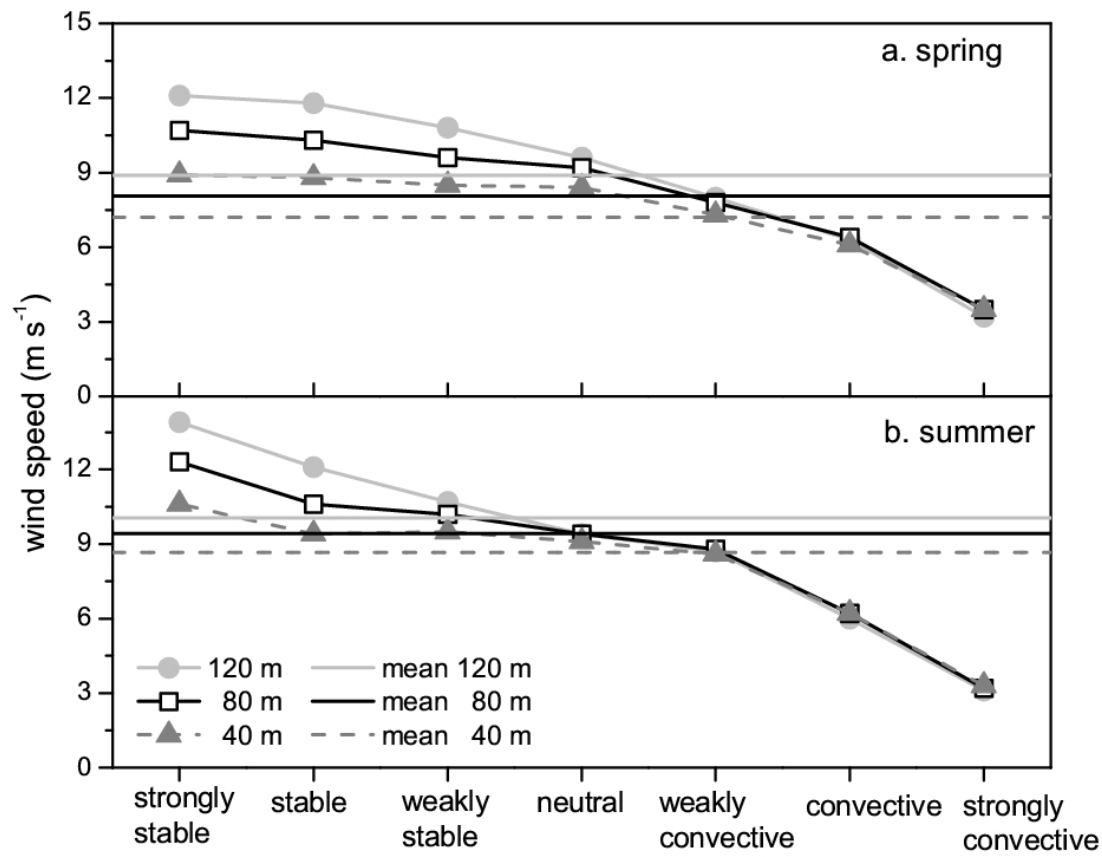
1166

1167 **Figure 9**

1168

1169

1170

1171

1172

1173

1174

1175

1176

1177

Figure 10

1178

1179

1180

1181

1182

1183

1184

1185

1186

1187

1188

1189

1190   **Figure 11**